

EXPERIMENTAL INVESTIGATION OF TURBULENT FLOW AND WIND  
COMFORT CHARACTERISTICS OF FRACTAL WIND FENCES

A THESIS SUBMITTED TO  
THE GRADUATE SCHOOL OF NATURAL AND APPLIED SCIENCES  
OF  
MIDDLE EAST TECHNICAL UNIVERSITY

BY

ŞEMŞİ ÇOŞKUN

IN PARTIAL FULFILLMENT OF THE REQUIREMENTS  
FOR  
THE DEGREE OF MASTER OF SCIENCE  
IN  
CIVIL ENGINEERING

JANUARY 2017



Approval of the thesis:

**EXPERIMENTAL INVESTIGATION OF TURBULENT FLOW AND WIND  
COMFORT CHARACTERISTICS OF FRACTAL WIND FENCES**

submitted by **Şemsi Çoşkun** in partial fulfillment of the requirements for the degree  
of **Master of Science in Civil Engineering Department, Middle East Technical  
University** by,

Prof. Dr. Gülbin DURAL ÜNVER  
Dean, Graduate School of **Natural and Applied Sciences**

Prof. Dr. Özgür Yaman  
Head of Department, **Civil Engineering**

Assoc. Prof. Dr. Özgür Kurç  
Supervisor, **Civil Engineering Dept., METU**

**Examining Committee Members:**

Prof. Dr. Kağan Tuncay  
Civil Engineering Dept., METU

Assoc. Prof. Dr. Özgür Kurç  
Civil Engineering Dept., METU

Assoc. Prof. Dr. Oğuz Uzol  
Aerospace Engineering Dept., METU

Assoc. Prof. Dr. Afşin Sarıtaş  
Civil Engineering Dept., METU

Asst. Prof. Dr. Burcu Güldür Erkal  
Civil Engineering Dept., Hacettepe University

**Date:** 19.01.2017

**I hereby declare that all information in this document has been obtained and presented in accordance with academic rules and ethical conduct. I also declare that, as required by these rules and conduct, I have fully cited and referenced all material and results that are not original to this work.**

Name, Last name: Şemsi Çoşkun

Signature :

## **ABSTRACT**

### **EXPERIMENTAL INVESTIGATION OF TURBULENT FLOW AND WIND COMFORT CHARACTERISTICS OF FRACTAL WIND FENCES**

Çoşkun, Şemsi

M.Sc., Department of Civil Engineering

Supervisor: Assoc. Prof. Dr. Özgür Kurç

January 2017, 64 pages

The characteristics of turbulent flow behind the fractal fences are rather new research area. Previous studies on fractal fences showed that there are clear differences in the flow characteristics as compared with the conventional fences. This study presents the results and comparisons of an experimental study that investigates the turbulent flow and wind comfort characteristics of fractal wind fences. Four different wind fences, three of which have fractal geometries, with the same height, width, and porosity ratio were tested. The experiments were conducted in a suction-type wind tunnel at the Center for Wind Energy, METU. Velocity field around the fences were measured with PIV technique and Reynolds number based on the fence height ( $Re$ ) was calculated as 53794. It is observed that in the near wake region, mean flow field characteristics such as streamwise and vertical velocity, vorticity, and turbulent flow characteristics are directly affected by the jet flows passing through the openings and bar wakes of the fractal fences. Although jet flow passing through the gaps of the conventional fence are quite uniform and mix out quickly, there are non-uniform jets at fractal fences which affect far downstream distances. Moreover, in order to investigate the wind comfort characteristics of the fences, two different dimensionless parameters which are wind speed reduction coefficient and shelter parameter are calculated. The results show that high degree of wind velocity reduction and shelter efficiency can be achieved by different fractal types of fences.

Furthermore, fractal fences may allow custom design of their fractal geometries according to the desired wind conditions in the downstream regions.

Keywords: Wind fence, Fractal design, Wake flow, Wind speed reduction coefficient, Shelter parameter

## ÖZ

### **FRAKTAL RÜZGAR BARIYERLERİNİN TÜRBÜLANSLI AKIŞ VE RÜZGAR KONFORU ÖZELLİKLERİNİN DENEYSEL İNCELENMESİ**

Çoşkun, Şemsi

Yüksek Lisans, İnşaat Mühendisliği Bölümü

Tez Yöneticisi: Doç. Dr. Özgür Kurç

Ocak 2017, 64 sayfa

Fraktal rüzgar bariyerlerinin arkasındaki türbülanslı akışın özellikleri oldukça yeni bir araştırma konusudur. Fraktal bariyerle ilgili önceki çalışmalar, geleneksel bariyerlerle karşılaştırıldığında, akış özelliklerinde belirgin farklılıklar bulunduğunu göstermiştir. Bu çalışma, fraktal rüzgar bariyerlerinin türbülanslı akış ve rüzgar konforu özelliklerini araştıran bir deneysel çalışmanın sonuçlarını ve karşılaştırmalarını sunmaktadır. Üçü fraktal geometri, aynı yükseklik, genişlik ve geçirgenlik değerlerine sahip dört farklı rüzgar bariyeri test edilmiştir. Deneysel, Orta Doğu Teknik Üniversitesi Rüzgar Enerjisi Teknolojileri Araştırma ve Uygulama Merkezindeki (ODTÜ RÜZGEM) emme tipi rüzgar tüneli içerisinde gerçekleştirilmiştir. Bariyerler etrafındaki hız alanı PIV tekniği ile ölçülmüş ve bariyer yüksekliğine dayanan Reynolds sayısı 53794 olarak hesaplanmıştır. Yakın çevre bölgesinde, akım doğrultusundaki ve düşey yöndeki ortalama hız ile vortisite gibi ortalama akış özelliklerinin; ve türbülans özelliklerinin, bariyerlerin açıklıklarından geçen jet akışlarından ve set girdaplarından doğrudan etkilendiği gözlemlenmiştir. Geleneksel bariyerin açıklıklarından geçen jet akışları oldukça düzenli olup hızlı bir şekilde karışsa da, fraktal bariyerlerin düzensiz jet akışları uzak mesafeleri etkilemektedir. Bariyerlerin rüzgar konfor özelliklerini araştırmak için rüzgar hızı düşürme katsayısı ve koruma parametresi olmak üzere iki farklı boyutsuz parametre hesaplanmıştır. Bu tezin çalışmasında elde edilen sonuçlar ışığında farklı

fraktal bariyer türleri ile yüksek düzeyde rüzgar hızı düşüşünün ve korunma verimliliğinin sağlanabileceği gösterilmiştir. Ayrıca, fraktal bariyerler, arkalarında istenilen rüzgar koşullarına göre fraktal geometrilerinin özel tasarımının da mümkün olabileceği anlaşılmıştır.

Anahtar Kelimeler: Rüzgar bariyeri, Fraktal tasarım, Çevrinti akıntısı, Rüzgar hızı düşürme katsayısı, Koruma parametresi

To my family

## ACKNOWLEDGEMENTS

This study was conducted under supervision of Assoc. Prof. Dr. Özgür Kurç. I would like to express my sincere gratitude for his guidance, continuous support, motivation and patience. Furthermore, I would like to express my sincere appreciation to Assoc. Prof. Dr. Oğuz Uzol for his contributions, advice, constructive criticism, and invaluable support through the research. Not only their academic backgrounds but also their professional discernment in each step of this study made valuable contributions in the finalization of this thesis.

Besides, I would like to thank my team-mate Hooman Amiri Hazaveh for his extraordinary support and efforts. We spent more than a month to finish the experiments of this thesis. In this period, he was always ready to help me patiently. With his passionate participation, the experimental work of this thesis was successfully conducted.

Also, I am deeply thankful to Assoc. Prof. Dr. Yalın Arıcı for his encouragement and supports.

I sincerely thank to Dr. Engin Karaesmen and Dr. Erhan Karaesmen for their invaluable guidance.

Finally, my greatest thanks goes to my family but especially to my mother Zöhre Çoşkun for their boundless energy and endless love.

## TABLE OF CONTENTS

ABSTRACT .....	v
ÖZ .....	vii
ACKNOWLEDGEMENTS .....	x
TABLE OF CONTENTS .....	xi
LIST OF TABLES .....	xiii
LIST OF FIGURES .....	xiv
LIST OF ABBREVIATIONS .....	xvii
CHAPTERS	
1 INTRODUCTION .....	1
1.1 Literature Review .....	2
1.2 Objectives and Scope .....	8
2 EXPERIMENTAL SET-UP AND MEASUREMENT DETAILS .....	11
2.1 Experimental Set-up .....	11
2.1.1 Wind Tunnel Facility .....	11
2.1.2 Wind Fence Design .....	12
2.2 Measurement Details .....	16
2.2.1 PIV Measurements .....	16
2.2.2 Uncertainty Estimates .....	18
3 RESULTS AND DISCUSSIONS .....	19
3.1 Empty Tunnel Flow Field (No-Fence Case) .....	20
3.2 Wake Flow Field of CSG Fence (Baseline Case) .....	22
3.3 Wake Flow Field Characteristics of Fractal Grid Fences.....	27

3.4	Wind Comfort Characteristics .....	45
4	CONCLUSIONS .....	59
	REFERENCES .....	63

## LIST OF TABLES

TABLES	
Table 2-1	Design parameters of conventional and fractal wind fence grids..... 14
Table 3-1	Summary of compared literature's parameters ..... 25

## LIST OF FIGURES

FIGURES	
Figure 2-1	Wind tunnel facility used in experiments ..... 12
Figure 2-2	Fence grid patterns: (a) regular, (b) fractal square, (c) fractal I and (d) fractal reverse-I..... 13
Figure 2-3	(a) Generated wind fences from top to bottom: conventional, fractal I, fractal reverse-I and fractal square, (b) fractal square fence in the wind tunnel ..... 15
Figure 2-4	Schematic representation of the experimental set-up ..... 17
Figure 2-5	Visualization of PIV measurement..... 18
Figure 3-1	Measurement planes: center planes shown with red color, 2 <sup>nd</sup> planes shown with blue color..... 19
Figure 3-2	Mean streamwise velocity component ( $u$ ) and (b) turbulent kinetic energy distributions for the empty tunnel case within the PIV measurement domain. .... 21
Figure 3-3	Mean streamwise velocity and (b) turbulent kinetic energy profiles at $x=0$ and $x=10$ for the empty tunnel case showing the distributions within the wall boundary layer. .... 22
Figure 3-4	(a) Mean streamwise velocity component ( $u$ ), (b) transverse velocity component ( $v$ ), (c) out-of-plane vorticity ( $\Omega_z$ ) and (d) turbulent kinetic energy ( $k$ ) distributions for the CSG fence case. .... 23
Figure 3-5	Comparison of the normalized streamwise velocity data of the current study with that of McClure [37] and Kim and Lee [29] at (a) $x=1H$ , (b) $x=2H$ , (c) $x=3H$ , (d) $x=4H$ and (e) $x=5H$ ..... 26
Figure 3-6	Normalized mean streamwise velocity distribution of (a) CSG, (b) FSG, (c) FIG (d) FRIG fences based on the center plane measurements ..... 27
Figure 3-7	Normalized mean streamwise velocity distribution of (a) CSG, (b) FSG, (c) FIG (d) FRIG fences based on the 2 <sup>nd</sup> plane measurements 29

Figure 3-8	Normalized mean streamwise velocity profiles at (a) $x=H$ , (b) $x=2H$ , (c) $x=4H$ and (d) $x=6H$ for CSG, FSG, FIG and FRIG fences based on the mid-plane measurements .....	32
Figure 3-9	Normalized mean streamwise velocity profiles at (a) $x=H$ , (b) $x=2H$ , (c) $x=4H$ and (d) $x=6H$ for CSG, FSG, FIG and FRIG fences based on the 2 <sup>nd</sup> plane measurements .....	33
Figure 3-10	Normalized mean transverse velocity distributions downstream of (a) CSG, (b) FSG, (c) FIG and (d) FRIG fences based on the center plane measurements .....	34
Figure 3-11	Normalized mean transverse velocity distributions downstream of (a) CSG, (b) FSG, (c) FIG and (d) FRIG fences based on the 2 <sup>nd</sup> plane measurements .....	35
Figure 3-12	Normalized mean transverse velocity profiles at (a) $x=H$ , (b) $x=2H$ , (c) $x=4H$ and (d) $x=6H$ ; for CSG, FSG, FIG and FRIG fences based on the mid-plane measurements .....	36
Figure 3-13	Normalized mean transverse velocity profiles at (a) $x=H$ , (b) $x=2H$ , (c) $x=4H$ and (d) $x=6H$ ; for CSG, FSG, FIG and FRIG fences based on the 2 <sup>nd</sup> plane measurements .....	36
Figure 3-14	Normalized mean out-of-plane vorticity distributions downstream of (a) CSG (b) FSG (c) FIG and (d) FRIG fences based on the center plane measurements.....	38
Figure 3-15	Normalized mean out-of-plane vorticity distributions downstream of (a) CSG (b) FSG (c) FIG and (d) FRIG fences based on the 2 <sup>nd</sup> plane measurements .....	39
Figure 3-16	Normalized turbulent kinetic energy distributions downstream of (a) CSG, (b) FSG, (c) FIG and (d) FRIG fences based on the center plane measurements .....	40
Figure 3-17	Normalized turbulent kinetic energy distributions downstream of (a) CSG, (b) FSG, (c) FIG and (d) FRIG fences based on the 2 <sup>nd</sup> plane measurements .....	42

Figure 3-18	Normalized turbulent kinetic energy profiles at (a) $x=H$ , (b) $x=2H$ , (c) $x=4H$ and (d) $x=6H$ ; for CSG, FSG, FIG and FRIG fences based on the mid-plane measurements .....	43
Figure 3-19	Normalized turbulent kinetic energy profiles at (a) $x=H$ , (b) $x=2H$ , (c) $x=4H$ and (d) $x=6H$ ; for CSG, FSG, FIG and FRIG fences based on the 2 <sup>nd</sup> plane measurements .....	44
Figure 3-20	Wind speed reduction coefficient (equation 3-2) distribution of (a) CSG (b) FSG (c) FIG and (d) FRIG fences based on center plane measurements .....	47
Figure 3-21	Wind speed reduction coefficient (equation 3-2) distribution of (a) CSG (b) FSG (c) FIG and (d) FRIG fences based on 2 <sup>nd</sup> plane measurements .....	48
Figure 3-22	Wind speed reduction coefficient distributions along $x/H$ at (a) $y=0.25H$ , (b) $y=0.50H$ , (c) $y=0.75H$ and (e) $y=1.0H$ based on center plane measurements.....	49
Figure 3-23	Wind speed reduction coefficient distributions along $x/H$ at (a) $y=0.25H$ , (b) $y=0.50H$ , (c) $y=0.75H$ and (e) $y=1.0H$ based on 2 <sup>nd</sup> plane measurements .....	50
Figure 3-24	Shelter parameter (equation 3-3) distributions of (a) CSG (b) FSG (c) FIG and (d) FRIG fences based on center plane measurements.....	52
Figure 3-25	Shelter parameter (equation 3-3) distributions of (a) CSG (b) FSG (c) FIG and (d) FRIG fences based on 2 <sup>nd</sup> plane measurements.....	54
Figure 3-26	Shelter parameter distributions along $x/H$ at (a) $y=0.25H$ , (b) $y=0.50H$ , (c) $y=0.75H$ and (e) $y=1.0H$ based on center plane measurements .....	55
Figure 3-27	Shelter parameter distributions along $x/H$ at (a) $y=0.25H$ , (b) $y=0.50H$ , (c) $y=0.75H$ and (e) $y=1.0H$ based on 2 <sup>nd</sup> plane measurements .....	56

## LIST OF ABBREVIATIONS

CSG	: Conventional Square Grid
$D_f$	: Fractal dimension
FSG	: Fractal Square Grid
FIG	: Fractal I Grid
FRIG	: Fractal Reverse-I Grid
H	: Height of the wind fence
k	: Turbulent kinetic energy
$L_0$	: Maximum bar length in fractal grid (bar length of the 1 <sup>st</sup> iteration)
$L_1$	: Bar length of the 2 <sup>nd</sup> iteration in fractal grid
$L_2$	: Minimum bar length in fractal grid (bar length of the 3 <sup>rd</sup> iteration)
N	: Number of successive iterations
PIV	: Particle Image Velocimetry
$R_{c_{\Delta x,y}}$	: Wind speed reduction coefficient
$R_L$	: Ratio of successive bar lengths
$R_t$	: Ratio of successive bar thickness
$t_0$	: Maximum bar thickness in fractal grid (bar thickness of the 1 <sup>st</sup> iteration)
$t_1$	: Bar thickness of the 2 <sup>nd</sup> iteration in fractal grid
$t_2$	: Minimum bar thickness in fractal grid (bar thickness of the 3 <sup>rd</sup> iteration)
$t_r$	: Ratio of thickest to thinnest bar thickness
$t_p$	: Thickness of perimeter

- $u_{\Delta x,y}$  : Time-average wind speed in the disturbed flow caused by the fence
- $u_{0\Delta x,y}$  : Time-average wind speed in the absence of fence
- $U_0$  : Mean streamwise velocity in the absence of fence
- $U_\infty$  : Free-stream wind velocity
- $u$  : Mean streamwise velocity
- $v$  : Mean transverse velocity
- $\beta$  : Porosity Ratio (%)
- $\Psi$  : Shelter parameter
- $\Omega_z$  : Mean out-of-plane vorticity

## CHAPTER 1

### INTRODUCTION

Wind exposure, i.e. high wind speed and turbulence, causes many problems from pedestrian comfort to wind erosion. Wind erosion is a dynamic process in which soil particle detaches from the land and are transported by wind. Even though, wind erosion can be considered as a natural phenomenon in deserts and beaches, in agricultural regions where soil cover is not enough, wind erosion reduces the soil moisture and organic matter content, thus endangers the agricultural production. In addition to such undesired conditions, wind erosion can negatively affect the air quality by increasing the amount of dust in air which may also cause respiratory health problems. At regions with dry and windy climates, such problems become even more vital. Wind exposure can also create wind-blown particle emissions to the environment from open areas and industrial sites where open aggregate conical piles exist to store granular materials. Especially, such piles may consist of industrial residuals or coal, particle emissions would not only cause health environmental problems but also it may cause loss of valuable goods. For such cases, the turbulence in the wind exposure must be reduced to overcome these issues.

At long span bridges or viaducts, high wind speed threatens life safety. Especially high cross wind speeds induce large lateral forces to vehicles that endangers their overall stability. In cold days, constant wind speed at the surface of the viaducts cause icing of the road. High wind speeds at public areas such as open shopping areas, restaurants, cafes cause significant pedestrian discomfort. According to Wise, the level of pedestrian discomfort begins with a wind speed of 5 m/s [1]. Melbourne states the wind speed of 15-20 m/s become dangerous for pedestrian

activities [2]. As a result, remedies that help controlling the wind speed as well as the turbulence are required.

One simple solution for the aforementioned problems are the wind fences. Wind fences are simple structures and actually obstacles which are placed at regions with high wind exposure. This way, they can not only reduce the wind velocity behind but also, provide a sheltered region. Wind fences can have different geometries. They can be solid rectangular walls or they can be porous with different hole shapes. Depending on the geometry of the wind fence, the flow behind it can have different characteristics. For example, solid wind fence can create a quiet region behind but causes highly turbulent flow even at the far downstream. Porous fences, on the other hand, develops longer quiet region with low turbulence but they are not as successful as the solid fences in terms of reducing wind speeds. Moreover, the shape of the holes significantly changes the flow pattern behind. Thus, a wind fence geometry that allows reducing the unwanted effects of wind exposure in a controllable manner is crucial.

## **1.1 Literature Review**

Wind fences have been used in many different areas. Basic application area of wind fences is to control wind erosion in agricultural areas. Due to reduction in wind speed with the use of such fences, the evaporation from the soil is decreased and soil aggregation and organic matter contents are enhanced [3]–[6].

The other important application area of wind fences is reducing aeolian deposition from a target region. This type of fences are specifically named as sand fences. They are used in deserts, on beaches or other places where control of aeolian sedimentation is needed [7]. As an example, previous studies revealed that blown sand problem along the highway crossing the Taklimakan Desert in China was

prevented by sand fences [8], [9]. Besides, it is important to control atmospheric dispersion of wind-blown dust particles from coal piles in open storage areas and coal-fired power plants because they cause air pollution and environmental problems [10]. Also, wind erosion cause large amounts of particle emissions from the aggregate in the storage areas which are open to atmosphere [11]. It was shown that an appropriate design of wind fences can decrease and control the particle emissions from storage areas [10]–[14].

Wind fences are also used to provide traffic safety under strong wind conditions especially on bridges and viaducts. In 2004, Charuvisit et al. stated that driving becomes difficult and accidents might occur due to miss-steering of drivers under strong cross wind conditions [15]. There are many studies on optimum design of the wind fences for transportation structures. These studies agree that wind fences can reduce the wind speed and therefore decrease the horizontal wind drag force and as a result provides a safer conditions for vehicles and pedestrians [15]–[18].

The effectiveness of the wind fences depends on several parameters such as porosity ratio, porosity distribution, fence height, orientation, width and spacing [19]. Among these parameters, porosity ratio is accepted as the most effective parameter [20], [21] which is defined as the ratio of the open area to the total area of a wind fence. However, recent studies reveal that if wind fences have the same porosity ratio, different geometric gap shapes make clear differences on the flow characteristics around barriers and on the overall effectiveness in terms of sheltering effect.

As well as porous wind fence serves many applications in practice, the resultant wake flow is investigated deeply in literature. From the fluid mechanics point of view, porous fences cause complex flow characteristics such as high shear rate, large pressure gradient, and high turbulence intensity in the near-wake region [12]. In 1967, Baltaxe [3] experimentally investigated the air flow patterns behind the model wind fences which had 25%, 38% and 50% porosity ratios. He concluded that wind fences behaved as aerodynamically bluff barriers when their porosity ratio was under

a critical level, which was approximated as 35%. The flow patterns of such fences showed a well-defined turbulent wake. These flow patterns are independent of the Reynolds number and vary with the drag coefficient of the fence. The transition of flow patterns Reynolds number independent from Reynolds number dependent at a level of porosity ratio between 25% and 38%. The similar distinction made by Castro in 1971 [22]. He measured the drag and shedding frequency to obtain mean velocity and turbulent intensity variations in the wake of perforated plates with Reynolds number ranging from  $2.5 \cdot 10^4$  to  $9.0 \cdot 10^4$  [23]. In his study, two distinct regimes of flow stated were observed. At low porosity ratio, a large scale separated flow dominated the wake and, at high porosity ratio, a clear vortex street did not exist.

Raine and Stevenson explains the aerodynamic action of a wind fence as follows the wind fence exerts a drag force to the wind flow, causing a net loss of momentum and thus provides sheltering effect [24]. They classified the wake flow into two regions: the 'quiet' zone dominated by the bleed flow through the gaps of barrier and the sheltered zone dominated by the displaced flow far downstream of the barrier. As the porosity ratio of the fence decreases, the bleed flow decreases and the drag force increases. Below a certain porosity ratio, a region of large scale separated flow exist behind the barriers. This critical porosity ratio is approximated as 30% [24], [22], [25], [26]. Raine and Stevenson's experimental results confirmed that porous wind fences gave better overall protection than solid fences because they caused greater turbulence in its wake which made them less effective for overall wind protection [9], [19], [24], [27], [28]. The measurements in this study; however, were obtained by hot-wire anemometer which cannot detect the reverse flow and thus, underestimated the turbulent intensities behind fences [29].

Perera [25] measured the velocity field behind perforated plates whose porosity ratios were ranged from 0.0% to 50% with pulsed-wire anemometer (PWA) which gave more accurate measurements against the hot-wire anemometer (HWA). He also stated that porosity ratio was the most influential parameter on the wake

characteristics behind the fences. According to Perera's [25] and Castro's [22] studies, as the porosity ratio of the fences increases, the recirculating bubble, which is the separated large scale recirculating airflow region located behind fence when the porosity ratio is less than a critical value, detaches from the fence, moves downstream and becomes smaller.

In 1999, Lee and Kim investigated the velocity and turbulence field behind four different fences which had 0.0%, 20%, 40% and 65% porosity ratios with the two-frame particle tracking velocimetry (PTV) method in a circulating water channel [12]. Their study showed that each wake flow except for solid one had two shear layer one of which was attributed to the separated flow from the top of barrier, whereas the second one results from the interaction between the bleed flow and the wall boundary layer developing along the channel bottom surface. They observed that as the porosity ratio increased, the turbulence intensity and Reynolds shear stress decreased. Also, the recirculating bubble behind fences disappeared when the porosity ratio was greater than 40%.

Kim and Lee investigated the structure of the turbulent shear flow around porous fences having different bottom gap ratio ( $G/H$ , where  $G$  is the height of bottom gap and  $H$  is the height of fence) with hybrid PTV technique [29]. They classified the flow field into three regions. The first one was the upper shear layer which was separated from the top of the fence. Although the upper boundary of this shear layer was independent from the gap ratio, lower boundary of the upper shear layer was affected from the gap ratio. The second region was a bleed flow and the third region was the lower shear layer developed from the bottom gap. Kim and Lee showed that turbulence intensity, Reynolds shear stress, turbulent kinetic energy increased in the lower shear layer for the gap ratio equal to or larger than 0.2. They stated that gap ratio of 0.1 gave the best shelter effect among different gap ratio values.

There are numerous studies in the literature which attempt to find the optimum porosity ratio for wind fences. For different types of application areas, different

porosity ratios are accepted as the optimum porosity ratio. Cornelis and Gariels stated that the efficiency of the wind fences in wind erosion process was directly related to the efficiency in the reduction of wind speed and turbulence intensity [19]. In their study, 20%-35% porosity ratios were accepted as the optimum values in terms of wind-velocity reduction. They found that an evenly distributed porosity resulted in the longest protected region with pretty much decrease in wind velocity reduction. Dong et al (2006). revealed that fences with 30%-40% were the most effective ratios to control wind erosion, but porous fences having 30%-60% porosity ratios resulted the maximum effective shelter distance depending on height of the fence [27]. In another study conducted by Dong et al. in 2007, optimal porosity ratio was defined as a critical porosity ratio above which the bleed flow was dominant and below which reversed flow became significant and this value was suggested as 20%-30% [9]. Therefore, in order to decrease the wind erosion, fence porosity ratio should be less than or equal to 40%.

In literature, majority of the studies examined the wind fences with conventional geometries. They were most commonly permeable fences with square, rectangular or circular holes. Other than these conventional geometries, different types of geotextiles were also used as windscreen [30]. Recent studies on fractal/multiscale generated turbulence shows interesting results. Fractal geometry implies the geometry which consists of small scales or copies of the whole. As a natural windbreak, trees can be considered as examples of fractal geometry that nature uses. To develop an understanding of turbulent flows and its mechanism several studies were conducted on fractal or multiscale objects and grids. In 2003, Staicu et al. investigated the turbulent wakes of fractal objects [31] with hot-wire anemometry. They found that although Reynolds numbers were comparable to those of fractal objects, turbulence intensities of fractal object were much larger than the non-fractal ones had. They concluded that self-similar refinements, which were geometric iterations, made the fractal objects better turbulence generators. In 2007, Hurst and Vassilicos investigated the turbulent flow generated by three different fractal family

which are cross, I and square fractals. They placed 21 planar grids at the entrance of two different wind tunnels and measured the wake flow with hot wire anemometry [32]. Their experiments showed that the generated turbulent flow's homogeneity, isotropy, and decay properties were strongly affected by fractal parameters such as fractal dimension  $D_f$ , the ratio of thickest to thinnest bar  $t_r$ , effective mesh size  $M_{eff}$ . As compared with the regular grid having same blockage ratio, fractal grids generate high turbulence intensities and larger Reynolds numbers. Also, homogeneity of the turbulent flow generated by fractal grids can be improved by increasing  $t_r$  and best homogeneity is achieved by space filling grids where  $D_f=2$ . It was shown that for space-filling fractal grids, there was a production region where turbulence build up and then it decayed exponentially. It was also stated that the distance where turbulence reached its maximum value,  $x_{peak}$ , can be controlled by changing the smallest thickness on the grid. Moreover, turbulence intensity can be tuned with different  $t_r$  values. After this extensive study, many possible application areas emerge for mixing, combustion, air brakes and flow control [33], because this study showed that the geometries of fractal grids can be modified in such a way that they can generate high turbulence intensities with low pressure drops or vice versa [34].

Laizet and Vassilicos explained the working principle of fractal grids [35]. They stated that contrary to regular grid in which all wakes meet their neighboring wakes at the same short distance from the grid, there were successive distances from the fractal grids where different same-size pairs of wakes meet in the case of fractal grid turbulence. Therefore, the fractal grid turbulence generation was distributed in the streamwise direction causing the turbulence to be less and smaller the pressure drop very near region behind the grid when compared to flow behind the regular grid with the same blockage ratio. Also, fractal grid caused much longer pressure recovery and much smaller turbulence decay.

In 2012, Keylock et al., investigated the wake flow of 1D multiscale fractal wind fences and compared the results with the conventional ones of the same porosity ratio

[36]. They stated that height, bottom gap, and porosity ratio parameters were not the only parameters that define the turbulence structure behind the wind fences. Beside these parameters, arrangement of the struts have an important effect on the structure of the wake. They also realized that multiscale forcing to the flow increased the turbulence production and dissipation rates. After this study, McClure conducted an experimental investigation of the turbulent flow induced by two different fractal wind fences [37]. First type was the replica of the Keylock's 1D fractal fence and then, she added a 2D multiscale fence which was very similar to cross grid presented in Vassilicos's study [32]. McClure showed that 2D fractal fence was the most effective one for wind speed reduction among 1D fractal and conventional fences. Also 2D fractal fences cause Reynolds shear stress to be higher near the surface. However, 1D fractal fence provided lower Reynolds shear stress which was preferred for preventing particle remobilization.

## **1.2 Objectives and Scope**

The main objective of this study is to investigate the possible use of fractal grids as wind fences. For this purpose, four different types of fractal fences, one has conventional porous grid and the other three has fractal geometries, are tested in the wind tunnel. Fractal geometries involve square, I, and reverse-I shapes. These geometries are determined in such a way that all fences have almost the same porosity ratio, i.e. 40%.

Wake flow characteristics behind the wind fence is measured by 2D PIV (Particle Image Velocimetry) system. The measurements are taken at two different planes, i.e. at the middle, and at the middle of the second iteration of the fractal grids. The measurements extend to a length that is equal to  $10H$ , where  $H$  is the height of the fence. The flow characteristics behind each fence are examined in detail and

compared with each other. Wind comfort parameters are also calculated and the performance of each wind fence in terms of wind speed reduction and shelter effect is discussed.



## CHAPTER 2

### EXPERIMENTAL SET-UP AND MEASUREMENT DETAILS

Four different wind fences, three of which have fractal geometries, are tested in an open-loop medium scale suction-type wind tunnel. The fractal fence geometries are designed in such a way that all fences have similar porosity ratios. For each case, the flow and turbulence characteristics within the wake region of each fence are obtained using two-dimensional Particle Image Velocimetry (PIV) measurements.

In this chapter, first, details of the experimental set-up such as wind tunnel facility and wind fence design are presented. Then, PIV measurement details are explained as the second section of this chapter.

#### 2.1 Experimental Set-up

##### 2.1.1 Wind Tunnel Facility

The experiments are conducted in an open-loop suction-type wind tunnel that has a test section with a 1 m x 1 m cross section and 8 m long located at the Center for Wind Energy, Middle East Technical University, Turkey. The walls of the wind tunnel are all made of transparent plexiglass to provide appropriate optical access for the laser and camera. The maximum free-stream wind velocity inside the wind tunnel is measured to be 25 m/s with a background turbulence intensity is less than 2%. Figure 2-1 shows a general picture of the wind tunnel.

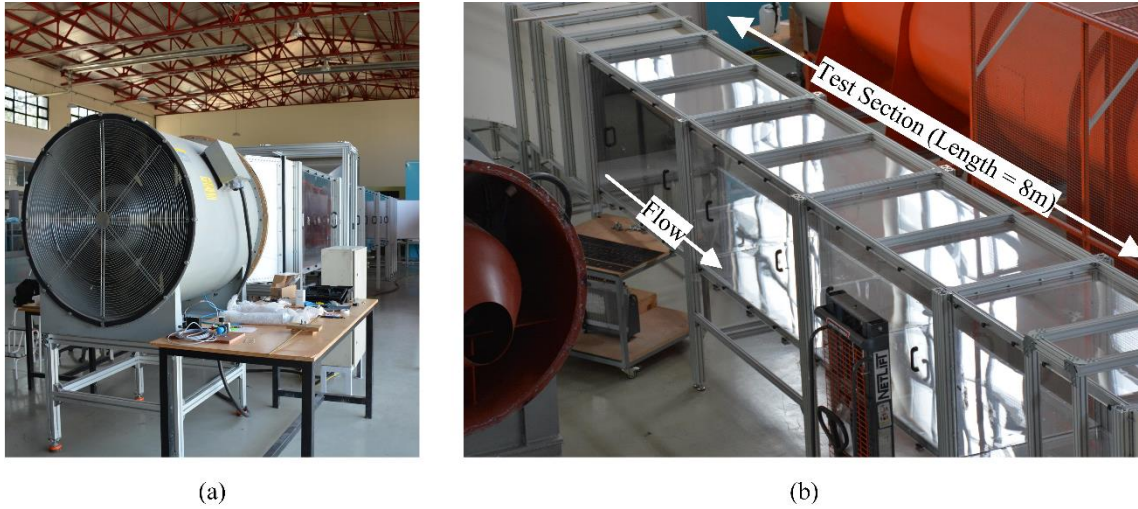


Figure 2-1 Wind tunnel facility used in experiments

### 2.1.2 Wind Fence Design

The fence grid patterns used in this thesis are presented in Figure 2-2. These are appropriately named as the Conventional Square Grid (CSG, Figure 2-2a), the Fractal Square Grid (FSG, Figure 2-2b), the Fractal I Grid (FIG, Figure 2-2c) and the Fractal Reverse-I Grid (FRIG, Figure 2-2d). The geometries of all fences are determined in such a way that they all have a porosity ratio that is close to 40%. This way, not only the reduction in wind velocity is targeted but also effect of fractal geometry on the flow characteristics are investigated.

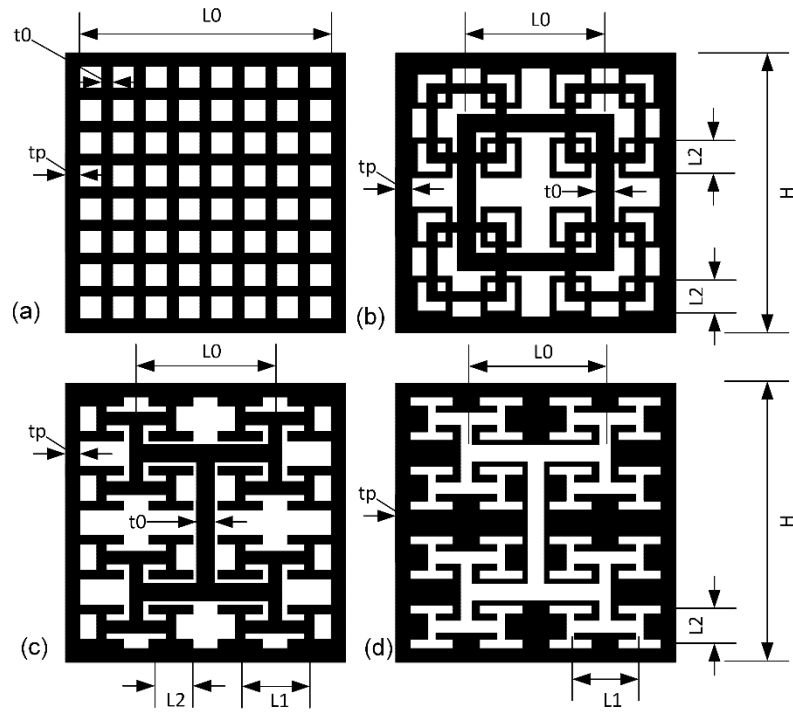


Figure 2-2 Fence grid patterns: (a) regular, (b) fractal square, (c) fractal I and (d) fractal reverse-I

As a starting point, every fractal grid was designed in such a way that they have the same iteration number, which is represented as  $N=3$ . Also, at each successive iteration, number of patterns i.e. square, I and reverse-I was increased by a factor of four ( $B=4$ ). Bar lengths ( $L_0$ ,  $L_1$  and  $L_2$ ) and thicknesses ( $t_0$ ,  $t_1$  and  $t_2$ ) shown in Figure 2-2 are calculated from Equation (2-1) and (2-2) respectively:

$$L_j = R_L^j L_0, \quad 0 \leq j \leq N - 1 \quad (2-1)$$

$$t_j = R_t^j t_0, \quad 0 \leq j \leq N - 1 \quad (2-2)$$

Therefore, by definition,  $L_0 \equiv L_{\max}$ ,  $L_2 \equiv L_{\min}$ ,  $t_0 \equiv t_{\max}$ ,  $t_2 \equiv t_{\min}$ . The ratio of successive bar lengths  $R_L$  and bar thicknesses  $R_t$  are defined in Equation (2-3) and (2-4):

$$R_L = \frac{L_{j+1}}{L_j}, \quad 0 \leq j \leq N - 1 \quad (2-3)$$

$$R_t = \frac{t_{j+1}}{t_j}, \quad 0 \leq j \leq N - 1 \quad (2-4)$$

In the presented designs,  $R_L$ ,  $R_t$ ,  $L_0$  and  $t_0$  are kept constant. Therefore, all fractal grids have the same fractal dimension ( $D_f$ ) as 2.0 calculated by Equation (2-5) as defined by Hurst and Vassilicos [38]:

$$D_f = \frac{\log(B)}{\log\left(\frac{1}{R_L}\right)} \quad (2-5)$$

The porosity ratio of each fractal grid is adjusted by changing the thickness ratio of the thickest to the thinnest bar ( $t_r = t_{\max}/t_{\min}$ ). Thickness of the perimeter ( $t_p$ ) is also adjusted to keep the fence heights the same. The parameters that define the fractal geometry are presented in Table 2-1.

Table 2-1 Design parameters of conventional and fractal wind fence grids

Grid Type	$\beta$ (%)	N	$R_t$	$R_L$	$D_f$	$t_r$	$t_0$ (mm)	$t_1$ (mm)	$t_2$ (mm)	$L_0$ (mm)	$L_1$ (mm)	$L_2$ (mm)	$t_p$ (mm)
Regular	40	1	1	0.5	2	1	4.26	4.26	4.26	100	100	100	5.5
Square	40	3	0.57	0.5	2	3.08	7.00	4.00	2.27	55	27.5	13.75	6.24
I	40	3	0.72	0.5	2	1.93	7.00	5.03	3.62	55	27.5	13.75	5.57
Reverse I	40	3	0.71	0.5	2	2.01	7.00	4.94	3.50	55	27.5	13.75	5.63

The height without perimeter ( $H'$ ) (see Figure 2-2) can be calculated as shown in Equation (2-6);

$$H' = L_0 + L_1 + L_2 + t_2 \quad (2-6)$$

Total solid area for fractal square grid pattern can be found with Equation (2-7):

$$A_{sq} = [H^2 - H'^2] + \sum_0^{N-1} B^j (SL_j t_j - St_j^2 + 4t_j^2) - \sum_0^{N-2} B^{j+1} (S-2)t_j t_{j+1} \quad (2-7)$$

For fractal I grid, Equation (2-8) can be used;

$$A_i = [H^2 - H'^2] + \sum_0^{N-1} B^j (SL_j t_j - St_j^2 + 4t_j^2) - \sum_0^{N-2} B^{j+1} (S-2) (t_j t_{j+1} + 0.5t_j (t_j - t_{j+1})) \quad (2-8)$$

In the case of fractal reverse-I grid, modified version of Equation (2-8) is also used. In this case, however,  $A_i$  represented the area of solid region.

Therefore porosity ratio,  $\beta$ , of the fences can be calculated from Equation (2-9);

$$\beta = \frac{A_{solid}}{H^2} \quad (2-9)$$

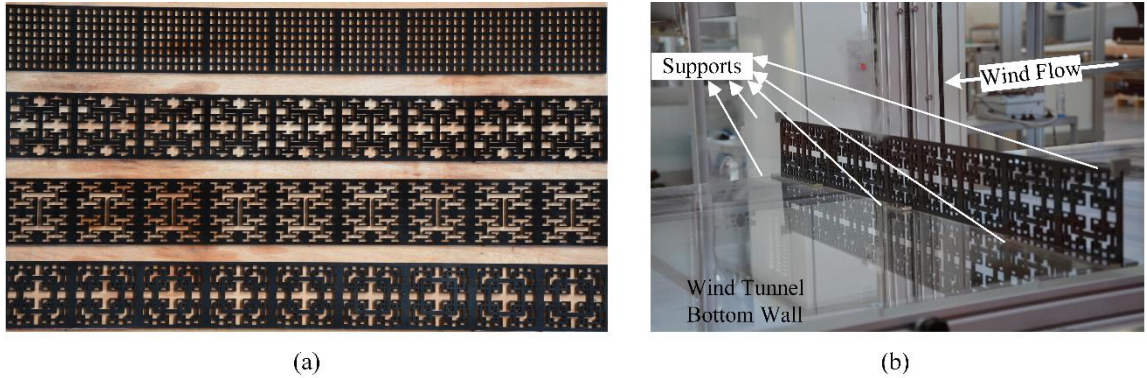


Figure 2-3 (a) Generated wind fences from top to bottom: conventional, fractal I, fractal reverse-I and fractal square, (b) fractal square fence in the wind tunnel

Fences were made from 4 mm thick transparent plexiglass material, cut in a CO<sub>2</sub> glass tube type laser cutting machine with a resolution of 0.5 mm. Also, in order to minimize light reflection; they were painted with opaque black spray paint shown in Figure 2-3 (a). The height (H) of the fences is 111 mm and the width (W) of the fences is 999 mm, covering almost the entire width of the tunnel. They were installed 215 cm downstream of the inlet of the wind tunnel test section. Because of wind force acting the fences, they were prone to display excessive bending. Therefore; from the same material, small pieces were used to support the fences as shown in Figure 2-3 (b). During the experiments, it is observed that the fences made inclinations due to horizontal wind force. This inclination angle measured minimum of 2.90 degrees for CSG fence and maximum of 3.60 degrees for FSG fence with the vertical axis. These inclination angles cause quite minor differences in experimental results.

## **2.2 Measurement Details**

Velocity field around the model wind fences were measured by two-dimensional Particle Image Velocimetry (PIV). In this section, details of PIV measurements and uncertainty estimates are explained.

### **2.2.1 PIV Measurements**

Figure 2-4 illustrates the experimental set-up layout schematically. The measurements are performed at a free-stream velocity of 8.6 m/s corresponding to a Reynolds number based on fence height of 53,793. Two-dimensional PIV technique is used to collecting data on multiple and slightly overlapping measurement windows (18 windows in total) as shown in Figure 2-4. The PIV measurements captured the

wind flow field between 1.3H upstream to 10.2H downstream from the fences in streamwise direction and 1.6H in the vertical direction, where H is the fence height.

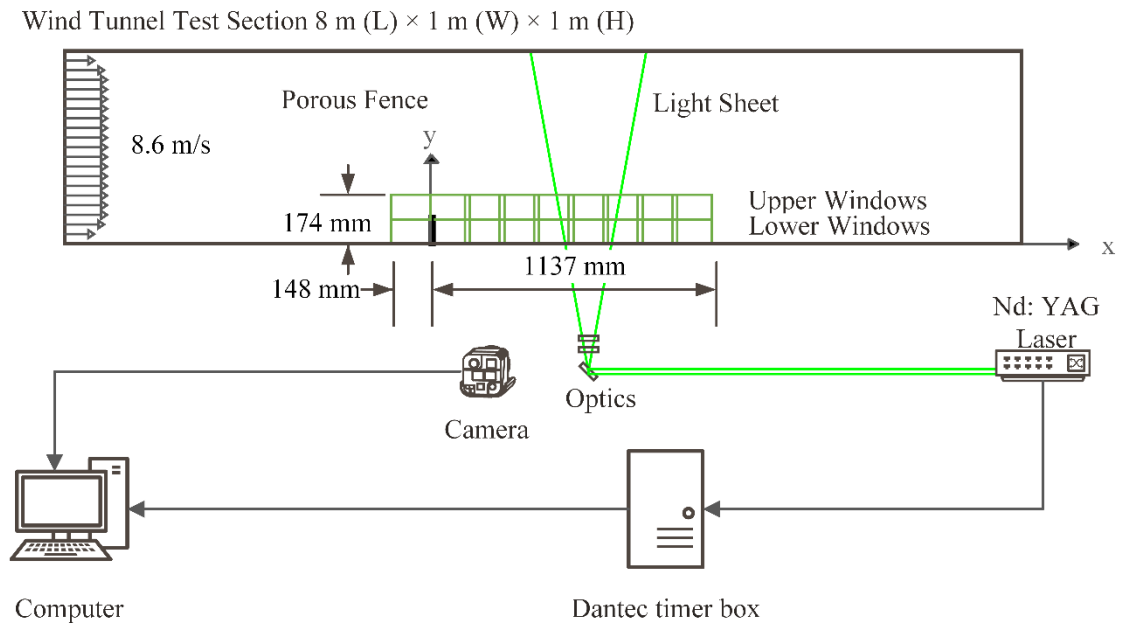


Figure 2-4 Schematic representation of the experimental set-up

The PIV system consist of a New Wave Solo Nd:YAG laser with a maximum power of 120 mJ/pulse, a hantom V640 12-bit 4MP resolution high speed camera equipped with 60 mm Nikon lens, a Dantec timer box and a computer with Dantec's Dynamic Studio software which are shown in Figure 2-5. The 532 nm green laser light is converted to a 2 mm thick laser sheet using a series of optics including a 500 mm focal length spherical, and a plano-concave 6.4 mm focal length cylindrical lenses. The laser sheet is then introduced into test section from the bottom of the tunnel using a 45 degree mirror. Olive oil droplets by a Laskin nozzle is used for flow seeding. The laser sheet and the camera are traversed to cover the total PIV measurement domain as shown in Figure 2-4.

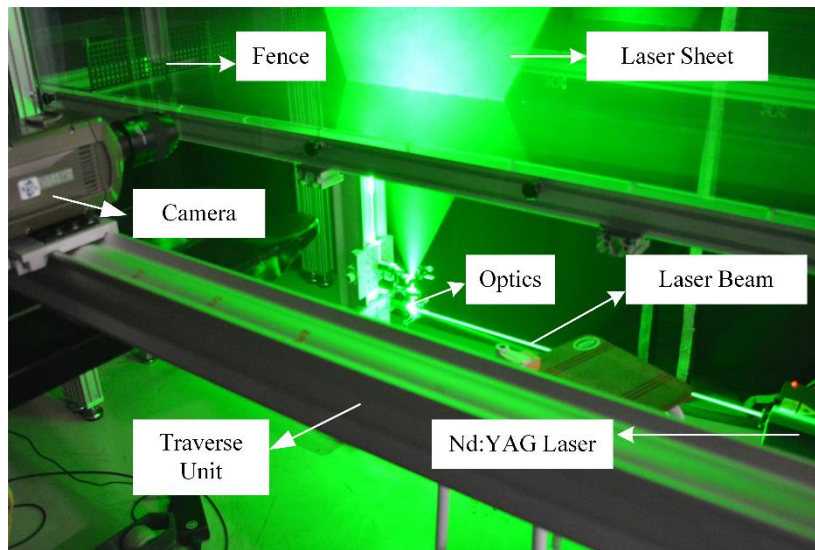


Figure 2-5 Visualization of PIV measurement

PIV image pairs are acquired with a time separation of  $60 \mu\text{s}$ . For each measurement window, a total of 1003 images are collected and used for statistical averaging calculations. The images are analyzed using  $32 \times 32$  pixels<sup>2</sup> interrogation windows with 50% overlap in both horizontal and vertical directions using cross correlation technique followed by moving average validation of  $3 \times 3$  neighborhood. The vector spacing in each measurement window is 1.0 mm.

### 2.2.2 Uncertainty Estimates

During the experiment, test section inlet velocity variation is less than 1%. The spatial displacement accuracy of the PIV cross-correlation algorithm is estimated to be less than approximately 0.1 pixel, which is expected to generate a spatial displacement error on the order of less than 1%. The sub-pixel accuracy is estimated to be around 0.3 pixels. The error result from temporal variations in the laser pulse synchronization is assumed as negligible. Traverse system was adjusted by hand during the experiment. Therefore the displacement accuracy is estimated to be less than 0.20 cm.

## CHAPTER 3

### RESULTS AND DISCUSSIONS

In this chapter, the results of the PIV measurements of a CSG fence as well as for three different fractal fences (i.e. FSG, FIG and FRIG fences are defined previously) are presented. First, a brief discussion on the results of the empty tunnel (no fence) case is presented as a reference, followed by the results and discussion of the baseline case which is the CSG fence in this thesis. Besides, comparisons with the results of the baseline case results with other recent experimental studies available in the literature are presented. Then, comparisons of the results obtained for the CSG fence with those of fractal fences are investigated, first regarding the wake flow details then focusing on the measured wind comfort characteristics.

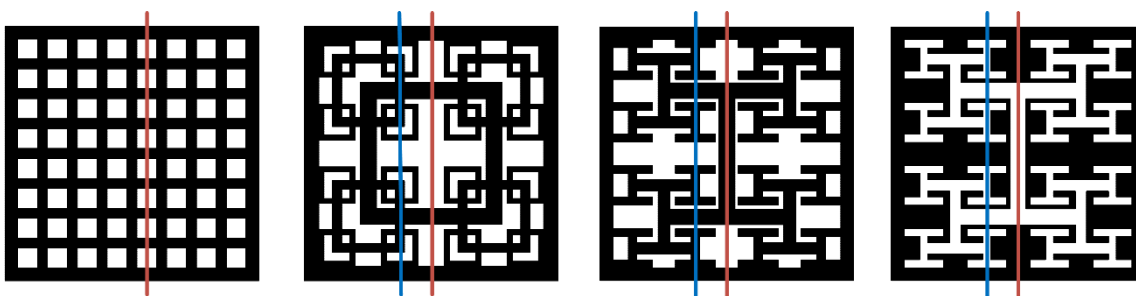


Figure 3-1 Measurement planes: center planes shown with red color, 2<sup>nd</sup> planes shown with blue color

The PIV measurements are based on two different set of experiments for the fractal fences. First set of experiments are conducted along the center planes which are labeled with red lines in Figure 3-1. Second set of experiments are on the other hand, based on measurements along the 2<sup>nd</sup> plane of the fractal fences which are labeled with blue in Figure 3-1. 2<sup>nd</sup> planes of fractal fences are selected in such a way that they intersect with the all three fractal iterations.

### 3.1 Empty Tunnel Flow Field (No-Fence Case)

The streamwise velocity component ( $u$ ) and the turbulent kinetic energy ( $k$ ) distributions for the empty tunnel, i.e. no-fence case are presented in Figure 3-2. Here, since we do not have the out of pane normal Reynolds stress component, i.e.  $\overline{w'^2}$ , the turbulent kinetic energy is approximated by assuming that  $\overline{w'^2}$  is the average of two available in-plane normal stress values, as described in [12]. So,

$$k = \frac{1}{2}(\overline{u'^2} + \overline{v'^2} + \overline{w'^2}) \cong \frac{3}{4}(\overline{u'^2} + \overline{v'^2}) \quad (3-1)$$

It should be kept in mind that this assumption will result in some error of approximated turbulent kinetic energy values where the flow is anisotropic, especially in the regions near the top edge of the fences. Also, the resultant flow field behind the fences are clearly turbulent and actually 2D assumption can make the turbulent kinetic energy calculation underestimate. Nevertheless, turbulent kinetic energy comparisons provide the comparison of the energies in the turbulent velocity fluctuations of the airflow passing through conventional and fractal wind fences.

Without any fence in the wind tunnel, the flow is quite uniform in the wind tunnel and the boundary layer growth along the wall can clearly be observed from Figure 3-2 (a). Boundary layer thickness is approximately 2.6 cm and 3.7 cm at  $x=0$  and  $x=10H$ , respectively, showing an approximately 42% increase in boundary layer thickness along the wall within the measurement domain.

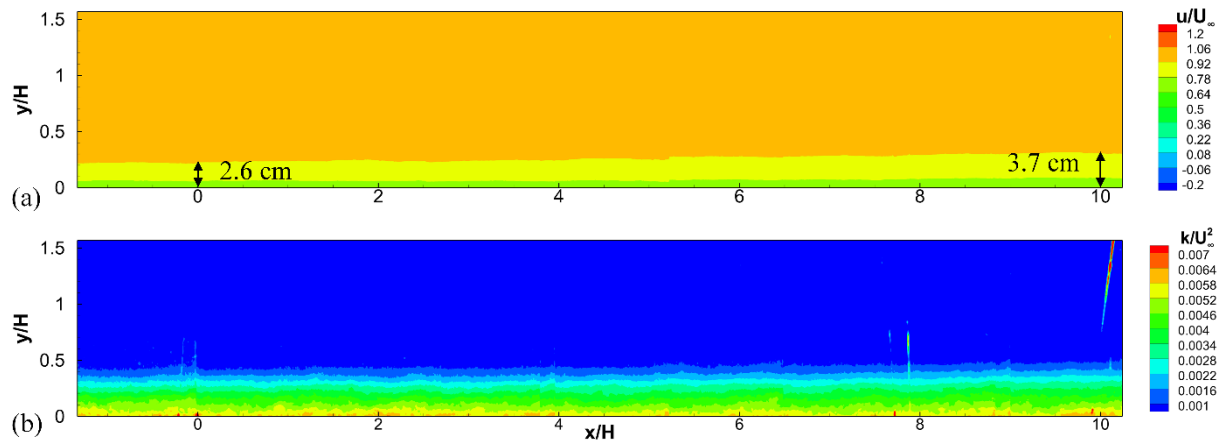


Figure 3-2 Mean streamwise velocity component ( $u$ ) and (b) turbulent kinetic energy distributions for the empty tunnel case within the PIV measurement domain.

The  $u$  and  $k$  profiles of the no-fence case (empty tunnel) are presented in Figure 3-3, comparing the variation along  $y/H$  at  $x=0$  and  $x=10H$ . The boundary layer growth is evident from the velocity profiles. The turbulence intensity within the free-stream is about 2% and goes up to 9% within the boundary layer when no fence is present.

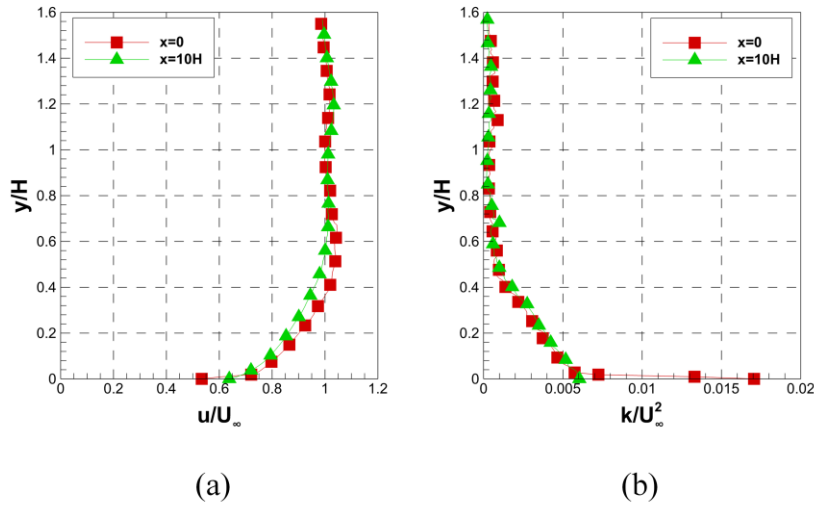


Figure 3-3 Mean streamwise velocity and (b) turbulent kinetic energy profiles at  $x=0$  and  $x=10$  for the empty tunnel case showing the distributions within the wall boundary layer.

### 3.2 Wake Flow Field of CSG Fence (Baseline Case)

The measurements on the conventional fence form the baseline study of present sets of experiments. Distribution of streamwise ( $u$ ) and transverse ( $v$ ) velocity components, out-of-plane vorticity ( $\Omega_z$ ) and turbulent kinetic energy ( $k$ ) are presented in Figure 3-4 (a) through (d). All parameters are normalized with proper reference values such as freestream velocity ( $U_\infty=8.6 \text{ m/s}$ ) and the fence height ( $H=111 \text{ mm}$ ). The blanked out region in these figures in the neighborhood of the fence is due to shadow zone of the fence, where laser illumination is not present. Keep in mind that the presented results are the statistical averages of 1003 PIV vector maps in respective windows.

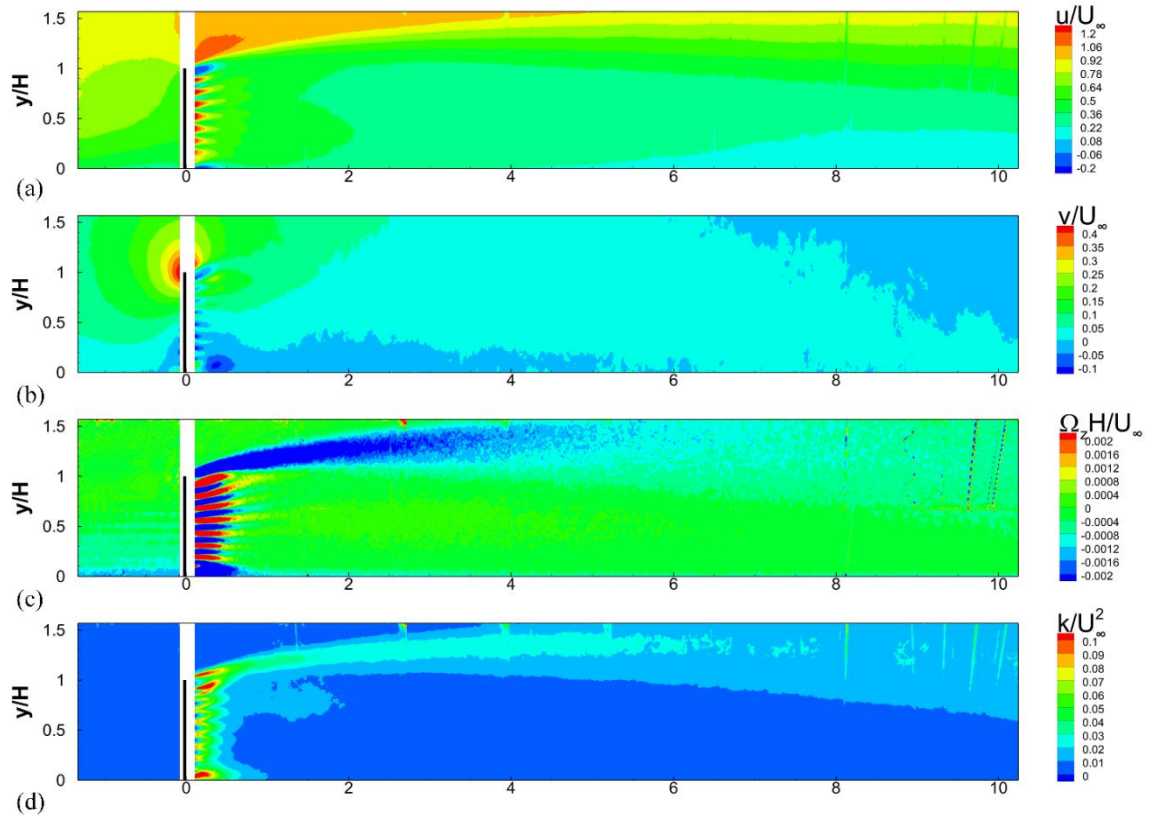


Figure 3-4 (a) Mean streamwise velocity component ( $u$ ), (b) transverse velocity component ( $v$ ), (c) out-of-plane vorticity ( $\Omega_z$ ) and (d) turbulent kinetic energy ( $k$ ) distributions for the CSG fence case.

Streamwise velocity contours in Figure 3-4 (a) show that the flow approaches to the fence, the streamwise velocity gets reduced due to potential field of the fence. However, flow velocity increases as it passing through the grid gaps and small jets are created just downstream of the fence exit. These jets are readily visible in the region  $x < 0.5H$ . The individual wakes of the grid bars are also observable in the same region. At the top of the fence and just at the corner, the flow quickly accelerates and a large wake zone is created downstream of the fence, even extending beyond the measurement domain at  $x=10H$ . The wake boundary trajectory is quite obvious from the contours such that it rises up to about  $x=5H$  and stays at that level further downstream. After about  $x=2H$ , the individual jets and wakes are not distinguishable

anymore and the flow become fully mixed creating one large low momentum wake zone. It can also be observed that after about  $x=5.5H$ , the wall boundary layer begins to grow near the tunnel bottom wall.

Mean transverse velocity contours are presented in Figure 3-4 (b). Except for the region where the fence is located, the transverse velocity is close to zero within a very large region inside the wake. Near the fence, regions with significant levels of transverse velocity such as near the top corner of the fence; where high positive values exist due to local flow turning; and near the wall just downstream of the fence, where high negative values can be obtained due to local influence of the fence all junction, which creates a step near the fence are observed.

The mean out-of-plane vorticity distribution given in Figure 3-4 (c) clearly shows two distinct regions downstream of the fence. A high negative vorticity band region created at the top corner of the fence and extending along the upper wake boundary trajectory and a region packed with positive-negative vorticity pairs just downstream of the fence marking the jets emanating through the gaps within the CSG fence. A high vorticity region near the wall just downstream of the fence due to step created by the fence-wall junction can also be observed. In these distributions negative vorticity is into the plane of the paper and is an indicator of strong vortex shedding with clockwise rotating vortices (for example, from the top corner of the fence and continuing along the upper wake boundary) due to the strong shear layer created at those regions. The diffusion of these high vorticity zones can also be observed as the wake region develops downstream of the fence and shear layers get weakened due to the mixing of the flow.

The turbulent kinetic energy distributions presented in Figure 3-4 (d) show that there are two important turbulence generation mechanism exist within the wake of the CSG fence. The first one is due to the shear layer initiated at the top corner of the fence. Due to existence of high velocity gradients in this shear layer, the turbulent kinetic energy gets maximized at the center of the shear layer along the upper wake boundary and the generated turbulence gets diffused as one travels further downstream. The second significant turbulence generation mechanism is due to the

interaction of the jets and bar wakes in the near wake region just downstream of the fence, as is evident from the  $k$  contours within the near wake region. After about  $x=2H$ , high turbulence that are created due to the interaction of the jets and wakes of the CSG fence seem to be fully mixed out, resulting in a reduction in the turbulent kinetic energy levels further downstream of the fence. The turbulence intensity level within this region is about 4.5%, slightly higher than the free-stream levels, which is about 2%.

Table 3-1 Summary of compared literature's parameters

Study	Porosity Ratio	Re Number	Facility	Bottom Gap
Current Study	40%	53794	Wind Tunnel	No
Kim and Lee (2002)	38.5%	8360	Water Channel	Yes
McClure (2016)	50%	36000	Wind Tunnel	Yes

Current PIV measurement results are also compared to similar CSG results in literature. Table 3-1 presents a summary of parameters defining the experimental conditions in all those studies. In McClure study [37], the porosity ratio of the fence is 50% and Reynolds number based on fence height is 36000 whereas in Kim and Lee [29] the fence porosity ratio and Reynolds number based on fence height are 38.5% and 8360, respectively. Unlike the present study, in both of those studies, there exists a bottom gap under the fence near the wall. Although McClure's experimental Reynolds number is closer to our case, it has been shown previously that the influence of porosity ratio is generally more dominant than the effect of the Reynolds number [22]. Therefore, a closer agreement of our data with Kim and Lee's results is expected.

Figure 3-5 compares the normalized velocity component distributions along  $y/H$  at different  $x/H$  locations downstream of the fence. As is evident, within the fence wake region where  $y/H < 1$ , all datasets are quite comparable to each other showing minor differences such as near the region next to wall, where a bottom gap is present in McClure as well as in Kim and Lee's data. As is expected, CSG fence of the present study shows a better agreement with Kim and Lee's results due to close porosity ratio levels, but still some differences can be observed due to existence of bottom gap, different Reynolds number levels and different experimental conditions because unlike the present study Kim and Lee were conducted their experiments in a circulating water channel. As one moves further downstream of the fence, McClure's study reveals higher streamwise velocity component values due to the big difference in porosity ratio levels.

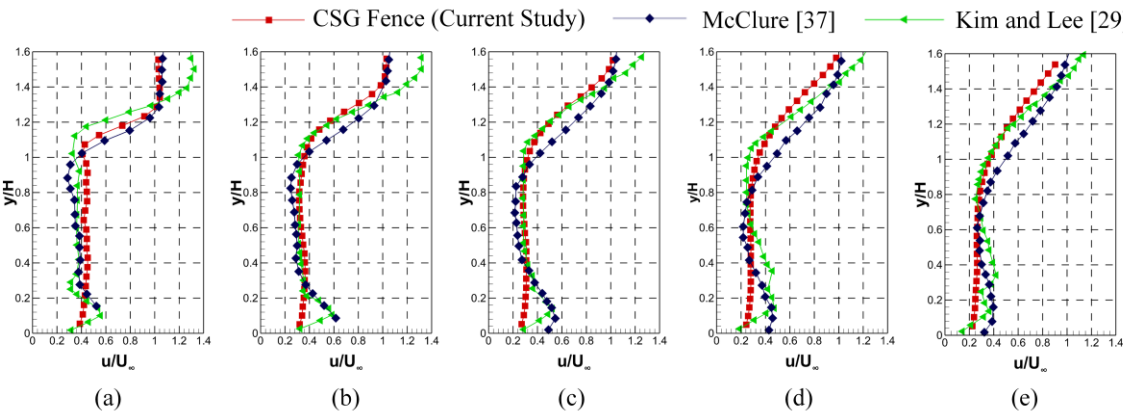


Figure 3-5 Comparison of the normalized streamwise velocity data of the current study with that of McClure [37] and Kim and Lee [29] at (a)  $x=1H$ , (b)  $x=2H$ , (c)  $x=3H$ , (d)  $x=4H$  and (e)  $x=5H$

### 3.3 Wake Flow Field Characteristics of Fractal Grid Fences

Figure 3-6 through Figure 3-19 show distributions of mean streamwise ( $u$ ) and transverse ( $v$ ) velocity components, out-of-plane vorticity ( $\Omega_z$ ) and turbulent kinetic energy ( $k$ ), respectively, for the CSG, FSG, FIG and FRIG cases. Corresponding fence grid shapes are included to the left of each contour plot for better understanding. The laser measurement planes are also marked in red on the fence grid shapes.

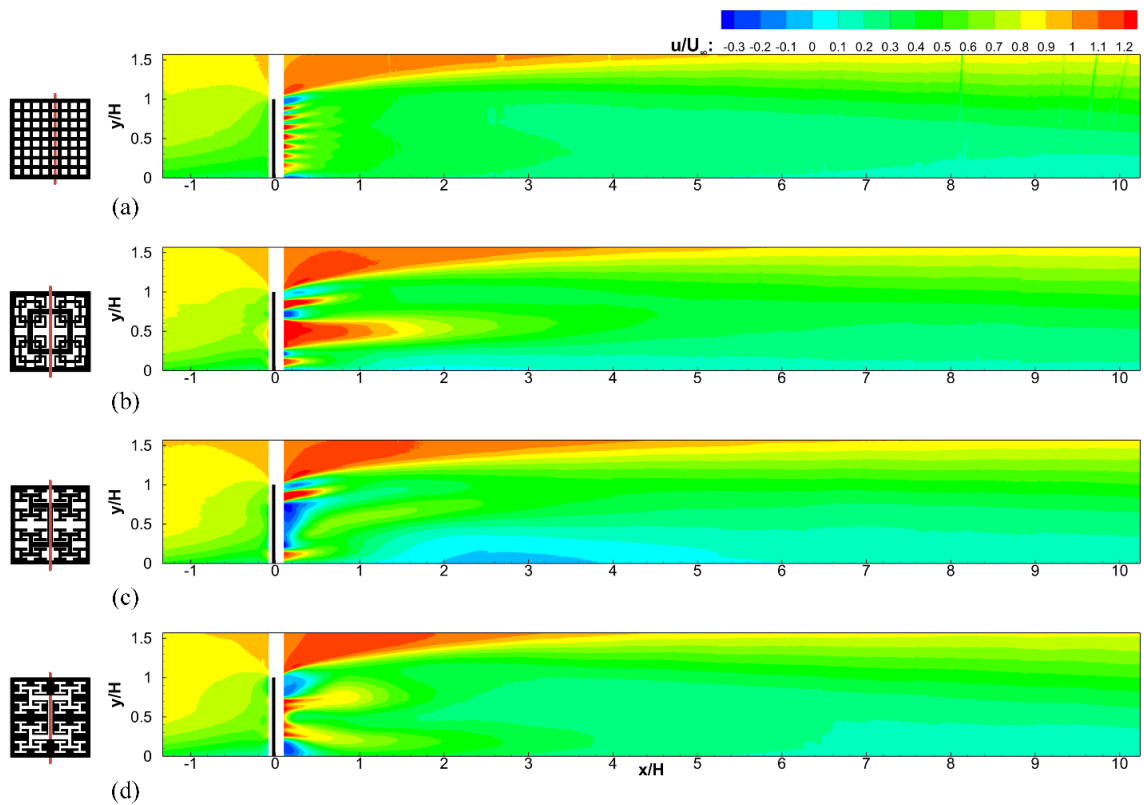


Figure 3-6 Normalized mean streamwise velocity distribution of (a) CSG, (b) FSG, (c) FIG (d) FRIG fences based on the center plane measurements

Fences are obstacles in the flow field so as the flow approaches the fences the velocity gets reduced upstream due to the potential effect of the grid, as is evident in Figure 3-6 and Figure 3-7. There are small differences in the  $u$  distributions just upstream of the fences. This is mainly due to the variations in local flow blockage created due to different grid shapes. Although all fences have the same overall blockage ratio of 60%, due to the fractal design of the fences, local blockage levels can be significantly different. One example is the mid-section of the FSG fence, where a large opening is presented, generating a much lower blockage compared with the same section of the CSG fence. The flow accelerates as it passes through the grid openings and when it is turning around the top corners of the fences. When compared with no fence case presented in Figure 3-2 (a), all four fences create significant amount of reduction in streamwise wind velocity based on both center and 2<sup>nd</sup> plane measurement in general, however with substantial differences in velocity distributions especially in the near wake region downstream of the fences.

Downstream of the fences, within the very near the wake region, varying jet and wake flow patterns can be observed along  $y/H$  for different fence types. Although this pattern is quite uniform for the CSG fence, the fractal fences create non-uniform patterns based on their respective geometry. For example, for the FSG fence, the large gap at its center plane creates a large jet, which can be seen in Figure 3-6 (b) at the center of the fence around  $y/H=0.5$  and extending up to about  $x/H=2$ , dominating the near wake flow region. As can be seen from Figure 3-6 (b), this jet is surrounded by the smaller wakes of the upper and lower bars of the bigger square shape at the center of the fence (smaller blue zones at the top and bottom of the dominant jet) as well as by two other smaller jets above and below the top and bottom bars of the bigger square at the center, respectively (again marked by red contours). The flow field above and below the dominant center jet is also not symmetrical due to the presence of the wall below such that the extent of the wake and the smaller jet below the center jet is much reduced compared to their counterparts that are above the center jet.

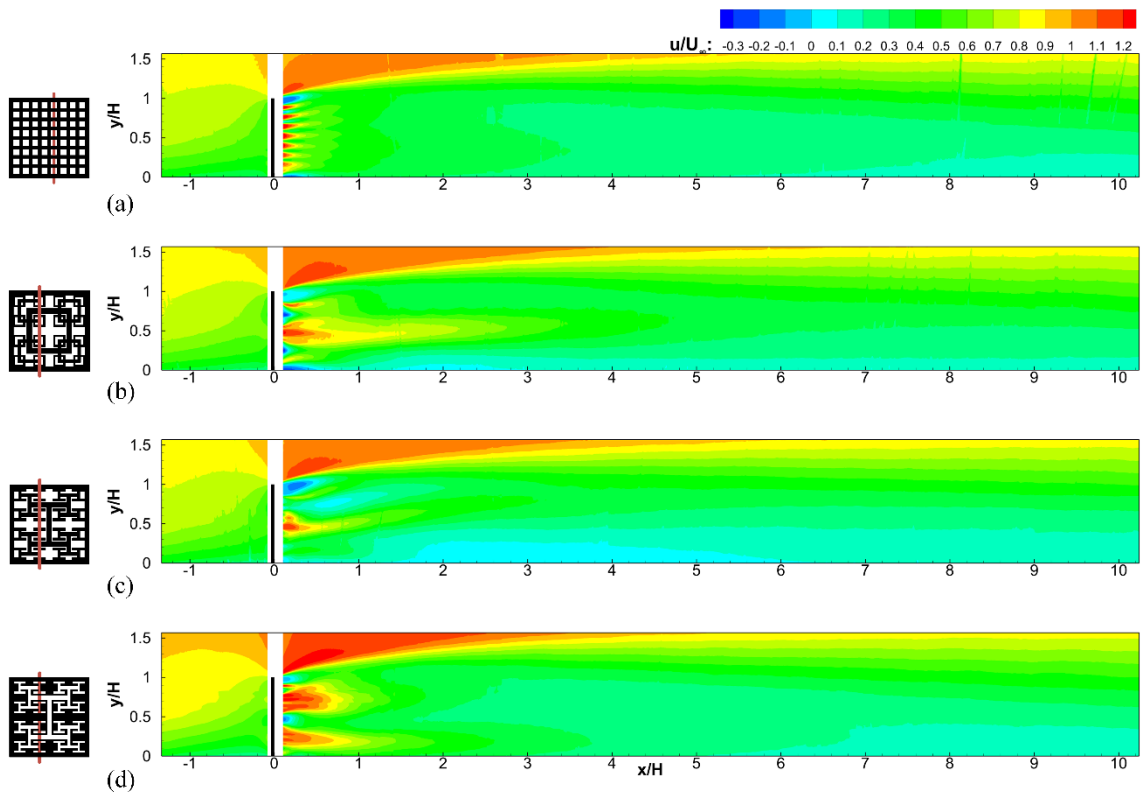


Figure 3-7 Normalized mean streamwise velocity distribution of (a) CSG, (b) FSG, (c) FIG (d) FRIG fences based on the 2<sup>nd</sup> plane measurements

On the other hand, along the 2<sup>nd</sup> plane, it is observed from Figure 3-7 (b) that the strength of the major jet decreases due to absence of intersection of the gaps of the biggest square. Also, bar wakes of the biggest square are still visible and shown with blue color. Besides, near the tunnel wall, intersection between perimeter and 3<sup>rd</sup> iteration square (smallest squares) creates a step, so a small recirculation zone resulted in a region  $0 < x < 0.5H$ . The interaction of this dominant center jet with surrounding smaller and asymmetric wake/jet flows in the near wake region is the main mechanism that determines the development of flow and turbulence characteristics further downstream of the fence. Note that all these non-uniformities are non-existent for the CSG fence and the jet/wake patterns created through the gaps and bars of the CSG fence get mixed out much quicker compared to the FSG or other

fractal grid fences. Individual jet/wake patterns become indistinguishable after about  $x/H=0.5$  for the CSG fence.

When compared with the FSG fence, the near wake flow field of the FIG fence is completely different. As presented in Figure 3-6 (c), the near wake flow field is dominated by the large wake generated due to the center I shape of the fence along the mid-plane. This wake is surrounded by two asymmetric jets corresponding to the upper and lower openings at the center plane of the FIG fence as well as the wake of the top and bottom bars of the fence. The asymmetric distribution around the center wake region creates non-uniform forcing on the wake making it much smaller and much quickly mixed out in the near wall region. In the near wake region downstream of the FIG fence, the center plane measurements and 2<sup>nd</sup> plane measurements are quite different than each other. There exist a small jet instead of wake along the 2<sup>nd</sup> plane because of the gap in the middle of the 2<sup>nd</sup> plane. Also, a small re-circulation zone occurs behind the top of the FIG along the 2<sup>nd</sup> plane. This is due to intersection of 3<sup>rd</sup> geometric iteration (smallest I shapes) and the perimeter.

The results presented in Figure 3-6 (d) show that the near wake of FRIG fence along its mid-plane is dominated by the wake of the center bar surrounded by two pairs of jets on each side of the wake emanating through the gaps above and below bar. These jet pairs get quickly combined together to form two strong jet regions above and below the center wake zone. The jet pairs are in turn surrounded by two big wake zones that are created by the geometrically blocked regions in the grid above and below the openings where the jets are created. Normalized streamwise contour plot of the FRIG based on the 2<sup>nd</sup> plane measurements are presented in Figure 3-7 (d). This time, in addition to jet flow caused by the gaps of biggest I shape, two more jets are observed due to gaps of smallest I shapes. On the other hand, symmetric wakes which are located top and bottom of the jets along its mid-planes are not visible along 2<sup>nd</sup> plane. Also, flow passing from the top of the FRIG has higher velocities along its 2<sup>nd</sup> plane, indicating a strong shear layer. It is interesting to note that the velocity field just downstream of the FRIG fence is much more symmetrical

compared to FSG or FIG fence cases, though small levels of asymmetry still can be observed.

The differences in the near wake regions of different fence types due to the creation of different dominant flow structures and their respective interactions with their corresponding asymmetric and non-uniform surrounding velocity fields in turn create substantial differences in velocity distribution further downstream. One clear example of this is the near the tunnel wall region of the FIG fence case between  $1 < x/H < 6$ , where a large low momentum zone gets created (there is even a region with negative  $u$  levels between  $2 < x/H < 4$  near the wall along its center plane), which is basically non-existent in this level for the CSG, FSG or FRIG fence cases. For the FSG fence, a very shallow low momentum zone seems to exist between  $1 < x/H < 3$  along mid-plane. The wall boundary layer is much thicker for the FIG fence beyond  $x/H > 6$  compared to all other cases based on both center plane and 2<sup>nd</sup> plane measurements. For the FRIG fence, the start of wall boundary layer growth is basically delayed to much further downstream location (around  $x/H > 5.5$ ) mainly due to the lower jet pair impingement on the wall along its center plane. For the 2<sup>nd</sup> plane results of FRIG, boundary layer growth begins around  $6H$  downstream of the fence. It is obvious that the differences that are generated further downstream of the fences have a major impact on the wind comfort characteristics as will be explained in detail later in this thesis.

In order to make more quantitative comparisons, Figure 3-8 and Figure 3-9 present vertical profiles normalized streamwise distributions at different  $x/H$  locations for all fence cases based on center plane and 2<sup>nd</sup> plane measurements, respectively. The profiles clearly show near wake differences as well as the progressive reduction of these differences due to mixing as one moves away from the fences. At  $x/H=1$  (Figure 3-8 and Figure 3-9 (a)), the CSG fence velocity field shows a quite uniform distribution from the wall up to about  $y/H=1.1$ , indicating the individual wakes and jets are already mixed out at this location. However, for the fractal fence cases, the non-uniformities in the velocity profile up to  $y/H=1$  is evident. These non-uniformities are not the same with each other due to the differences in the flow

structures as discussed in the previous paragraphs. The evidence of the strong centrally dominant jet for FSG, the wake and jet combination of FIG and two symmetrical jet configuration of FRIG fences along their central planes can be all depicted from Figure 3-8 (a). Also along the second planes, the decrease in the strength of the major jet of the FSG, strong negative  $u$  distribution at the top of the FIG fence and symmetrical jets of FRIG fences are shown in Figure 3-9 (a).

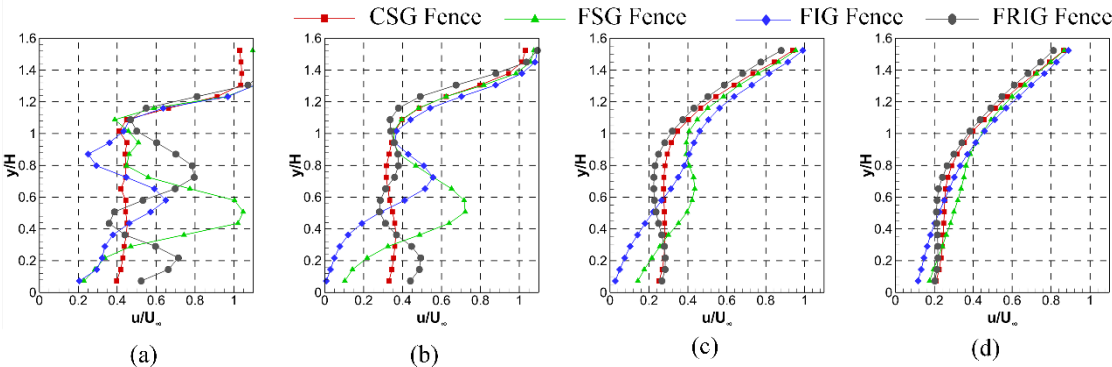


Figure 3-8 Normalized mean streamwise velocity profiles at (a)  $x=H$ , (b)  $x=2H$ , (c)  $x=4H$  and (d)  $x=6H$  for CSG, FSG, FIG and FRIG fences based on the mid-plane measurements

Note that for all fence cases, above  $y/H=1$ , all velocity profiles collapse on top of each other creating a sharp velocity gradient to reach the free-stream levels. As one move downstream, it is observed that the FRIG velocity profiles is the quickest one among others to converge to the values of the CSG fence, as shown in Figure 3-8 (c) and (d) as well as in Figure 3-9 (c) and (d). The FSG and FIG fences still show significant differences compared to CSG and FRIG cases at  $x/H=4$  (Figure 3-8 (c) and Figure 3-9 (c)). Though reduced, these differences do exist even at  $x/H=6$  (Figure 3-8 (d) and Figure 3-9 (d)). As explained previously, the large reduced momentum region near the tunnel bottom wall for the FIG fence is also visible from the profiles. For example, at  $x/H=4$  the velocity levels near the wall for FIG case are

reduced down to 80% of the levels of CSG fence, indicating a good potential for wind reduction applications.

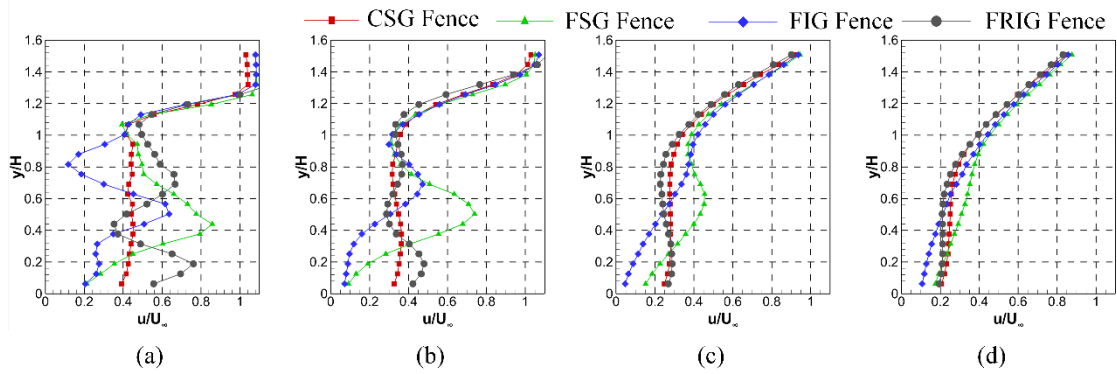


Figure 3-9 Normalized mean streamwise velocity profiles at (a)  $x=H$ , (b)  $x=2H$ , (c)  $x=4H$  and (d)  $x=6H$  for CSG, FSG, FIG and FRIG fences based on the 2<sup>nd</sup> plane measurements

Figure 3-10 and Figure 3-11 show contours of normalized mean transverse velocities for all fences along center and second plane, respectively. An immediate observation is that the transverse velocity levels are generally significant within the near wake regions of the fences, up to about  $x/H=2$ . After this location, the levels are very close to zero in general. In the region  $0 < x/H < 2$ , different fences exhibit different distributions of transverse velocity. For example, the CSG fence displays a quite uniform distribution behind the fence except for the near wall region, where a small re-circulatory zone exists due to the small step created at the fence-wall junction at the bottom wall Figure 3-10 and Figure 3-11 (a). For the FSG fence, the transverse velocity levels are relatively low, except within  $y/H < 0.25$  along the center plane shown in Figure 3-10 (b).

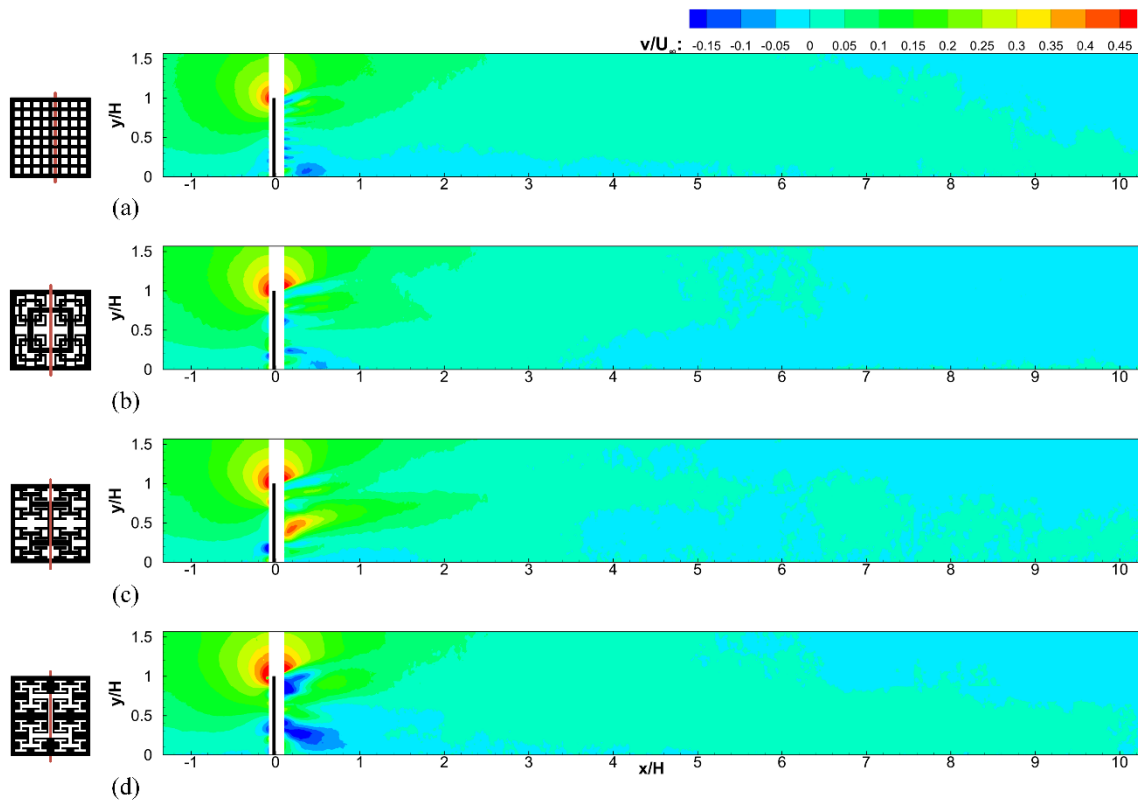


Figure 3-10 Normalized mean transverse velocity distributions downstream of (a) CSG, (b) FSG, (c) FIG and (d) FRIG fences based on the center plane measurements

However, second plane measurements of the FSG shows two distinct region where transverse velocities are negative (Figure 3-11 (b)). One of the regions is located behind the fence below its mid-height and the second one is located behind the fence at the top. Based on center-plane measurements, highest transverse velocity levels are observed for the FIG and FRIG cases, just downstream of the fences. A strong positive  $v$  region exists for the FIG fence at around  $0.25 < y/H < 0.5$  (Figure 3-10 (c)), whereas two strong negative regions are observed for the FRIG fence, one near the top of the fence and one near the wall which are shown in Figure 3-10 (d). For the second plane of FRIG fence, negative transverse velocity region appeared near the top does not exist, but one located near the wall still visible (Figure 3-11 (d)).

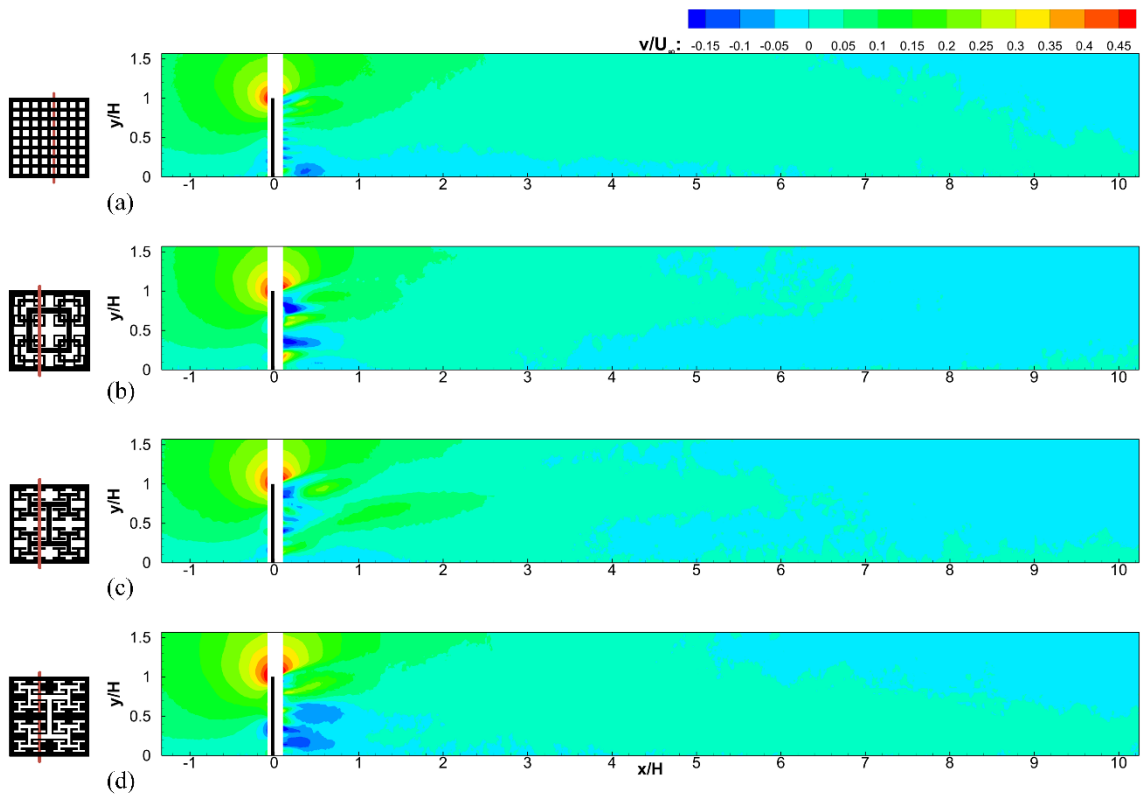


Figure 3-11 Normalized mean transverse velocity distributions downstream of (a) CSG, (b) FSG, (c) FIG and (d) FRIG fences based on the 2<sup>nd</sup> plane measurements

The positive  $v$  region shown in center plane results for the FIG fence is most probably responsible for lifting the flow upward from the wall, as described previously. In an opposite manner, the high negative regions near the wall of FRIG fence, which is mainly due to impinging jet on the wall, increases the momentum of the flow near the wall further downstream.

Figure 3-12 and Figure 3-13 show profiles of transverse velocity at different  $x/H$  location downstream of the fences. At the  $x/H=1$ , the strong positive transverse velocity levels of the FIG fence and negative levels of the FRIG fence are readily visible in the results of both center and second plane which are shown in Figure 3-12 (a) and Figure 3-13 (a), respectively.

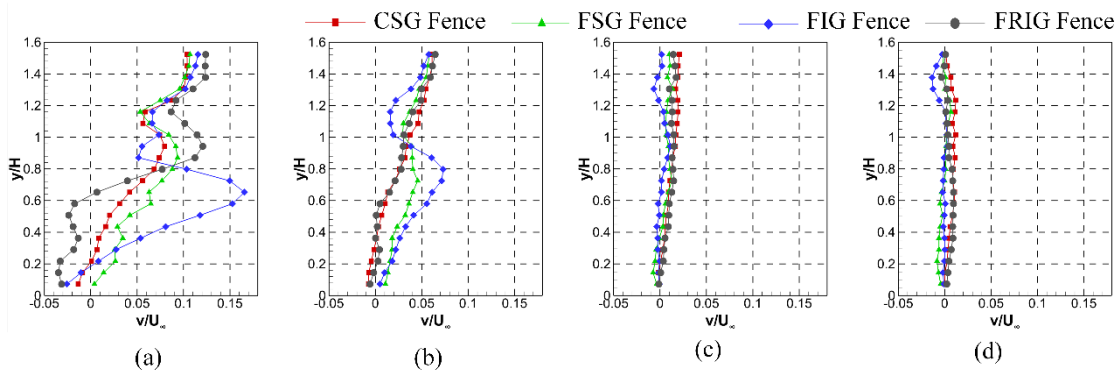


Figure 3-12 Normalized mean transverse velocity profiles at (a)  $x=H$ , (b)  $x=2H$ , (c)  $x=4H$  and (d)  $x=6H$ ; for CSG, FSG, FIG and FRIG fences based on the mid-plane measurements

The CSG and FRIG profiles are on top of each other even at  $x/H=2$  (Figure 3-12 (b) and Figure 3-13 (b)), but the transverse velocity distributions of the FSG and FIG show differences. As explained previously, the transverse velocity levels for all fences collapse on top of each other after  $x/H=4$ , and are almost zero within the wake zone.

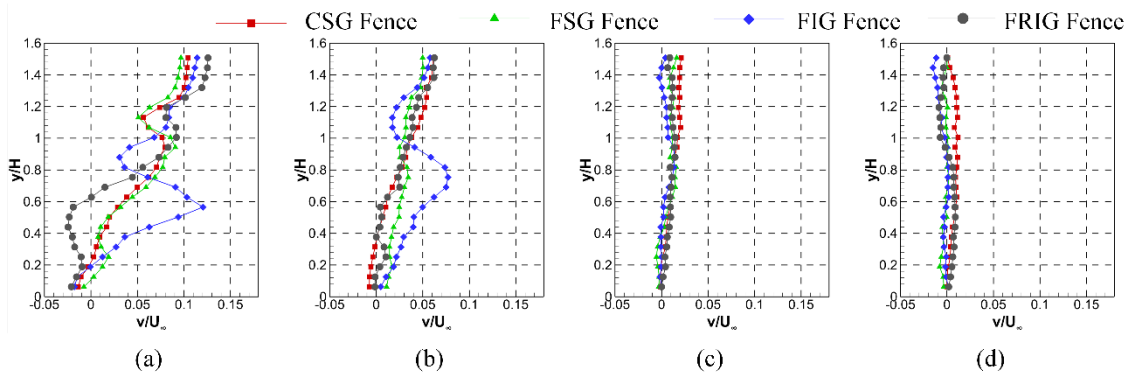


Figure 3-13 Normalized mean transverse velocity profiles at (a)  $x=H$ , (b)  $x=2H$ , (c)  $x=4H$  and (d)  $x=6H$ ; for CSG, FSG, FIG and FRIG fences based on the 2<sup>nd</sup> plane measurements

The details of the near wake flow structures that are discussed previously can readily be observed from the out-of-plane vorticity distributions presented in Figure 3-14 and Figure 3-15. In these plots, red-blue (i.e. positive-negative) vorticity pairs (red at the top and blue at the bottom) correspond to jet created through the gaps of various fences. The red (positive) and blue (negative) vorticity contours indicate counter-clockwise and clockwise rotation of fluid particles, respectively. It is clear that one of the important property of turbulent flow is that they are rotational, which means they have nonzero vorticity [39]. In the near wake region, all fractal grids show higher vorticity values than conventional fence's vorticity values. This can be seen a sign of an increase in turbulence level. It is important to note that different scales of bars which is the case of fractal fences directly affect the local spinning of the fluid particles.

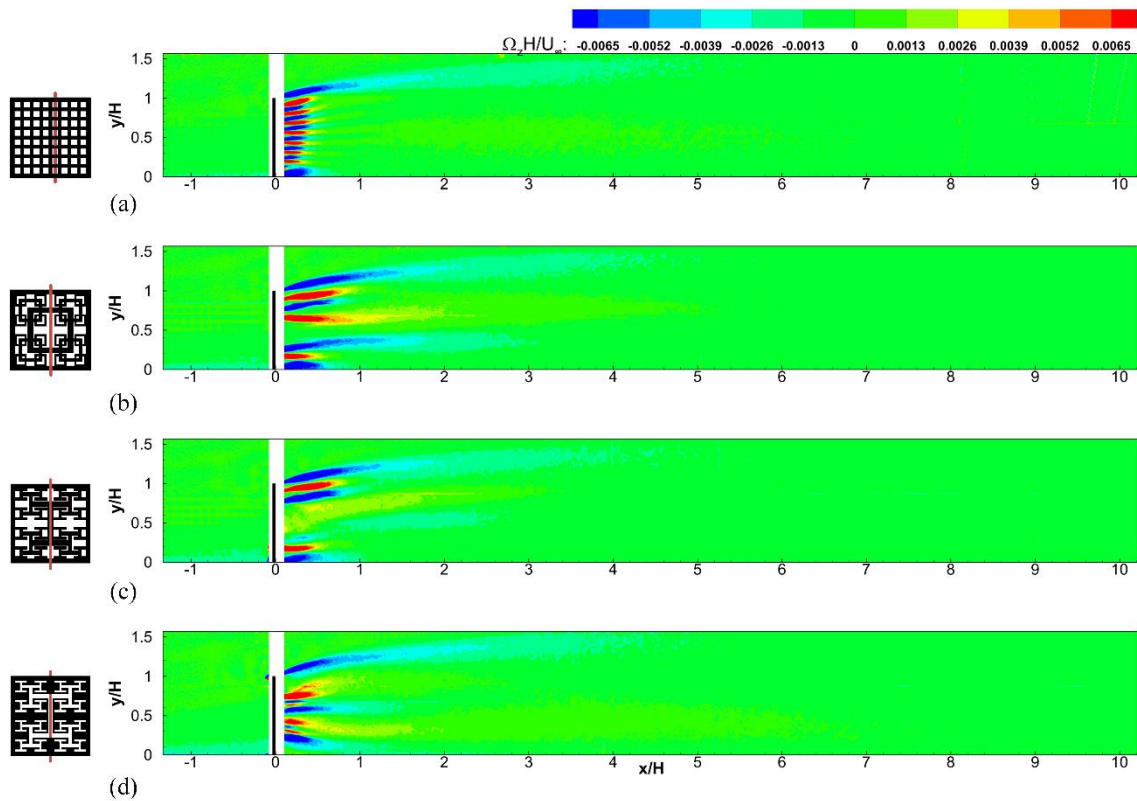


Figure 3-14 Normalized mean out-of-plane vorticity distributions downstream of (a) CSG (b) FSG (c) FIG and (d) FRIG fences based on the center plane measurements

Along the center plane of FSG fence, three major flows within the dominant jet at the center are marked with three pairs of red-blue vorticity contours from the top of the fence toward the wall of the bottom (Figure 3-14 (b)). On the other hand, for the second plane of FSG, due to small iterations of square shapes, the number of vorticity pairs increase and their strength are not high as the central ones. The top jet is directed upwards most probably due to the entrainment effect of the strong shear layer created at the top corner of the fence. This effect can also be observed for the CSG and FIG fences near the top such that the jets near this region always gets lifted upwards towards free-stream. Of course this changes the interaction of the jets near the top with the flow structures that exist at lower  $y/H$  levels.

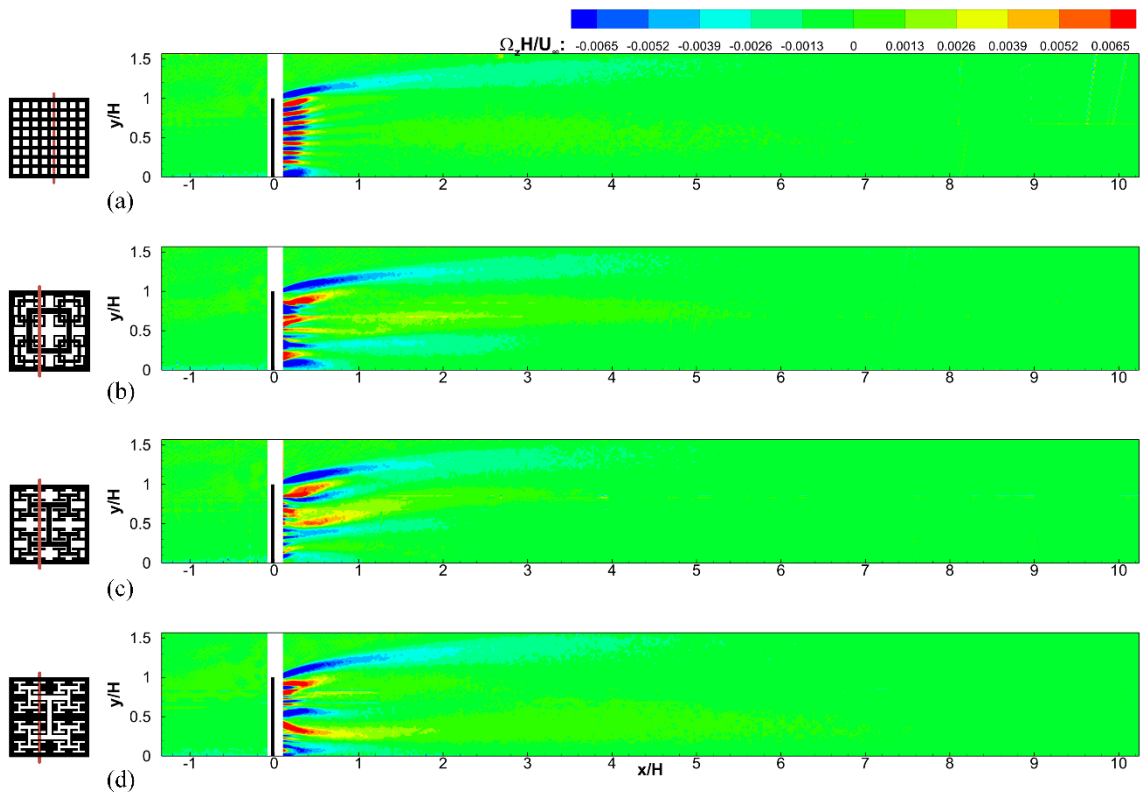


Figure 3-15 Normalized mean out-of-plane vorticity distributions downstream of (a) CSG (b) FSG (c) FIG and (d) FRIG fences based on the 2<sup>nd</sup> plane measurements

The interaction of different flow structures within the near wake has an impact of downstream flow characteristics, however the vorticity levels after about  $x/H=4$  are very close to zero. In addition to the distributions of vorticity, the actual magnitude of out-of-plane vorticity also shows significant variations from fence to fence. In near wake region, all fractal grids show higher vorticity levels than those of the conventional fence such that the magnitude of out-of-plane vorticity of the fractal fences is at least about four times higher than that of the conventional fence.

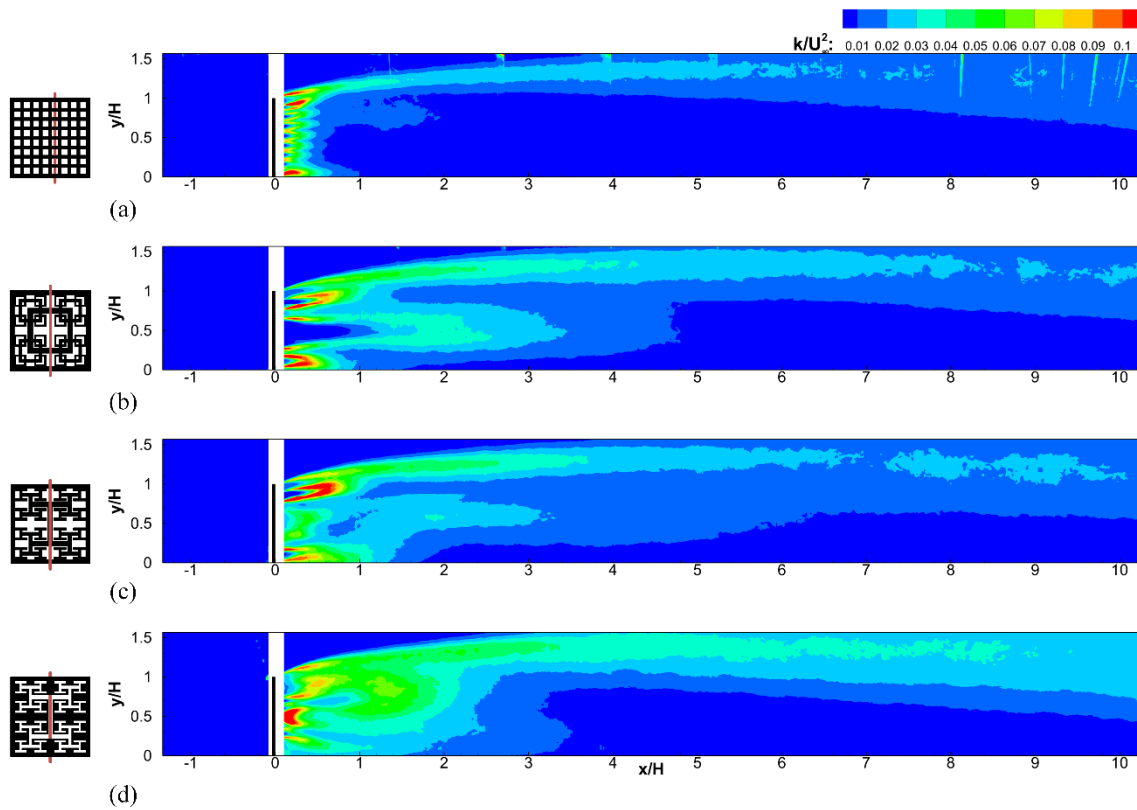


Figure 3-16 Normalized turbulent kinetic energy distributions downstream of (a) CSG, (b) FSG, (c) FIG and (d) FRIG fences based on the center plane measurements

Turbulent kinetic energy distributions within the wakes of CSG and fractal grid fences are presented in Figure 3-16 and Figure 3-17 based on center and second plane measurements, respectively. It can be seen from these two figures that the turbulence levels and respective distributions downstream of the fences show significant differences among different types of fences, mainly due to completely different turbulence generation mechanism that exist within the near wake region. For CSG fence (Figure 3-16 and Figure 3-17 (a)) high turbulence is generated through the jets and wakes of regular turbulence grid, which are very quickly mixed out and after about  $x/H=1$  the turbulent kinetic energy levels within the wake become very uniform and almost as low as free-stream levels.

On the other hand, for fractal fences in general, the high turbulence regions downstream of the fence can extend beyond  $x/H=3$ , depending on the fractal type. The fractal geometry also influences the level of turbulence within the strong shear layer that is initiated at the top corner of the fence. Along its center plane for the FSG fence, the main turbulence generation mechanism is due to two local shear layers that are created on either side of the large center jet as well as due to the interaction of the large center jet with two smaller jets surrounding it. The core region of large center jet seem to have a low turbulence potential region, which is enclosed on either side by two high turbulence zones which in turn start mixing with each other further downstream. The influence of large center jet on the turbulence field can be observed even until  $x/H=4.5$ , after which the levels are significantly reduced based on its center plane measurements. The turbulence levels near the wall are generally low after  $x/H=1$ . The high turbulence shear layer along the wake boundary at the top is thicker compared to the CSG case, mainly due to extra injection of turbulence in to the shear layer from the small upper jet near top of the fence, as shown in Figure 3-16 (b). According to 2<sup>nd</sup> plane measurements (Figure 3-17 (b)), turbulence level in the upper shear layer along the wake boundary is higher than those measured along the center plane. This high turbulence level in the upper shear layer extends more downstream distances up to about  $8H$  along the second plane, whereas it reaches about  $4H$  downstream distance along its center plane. On the other hand, distribution of turbulent kinetic energy in the near wake zone based on 2<sup>nd</sup> plane measurement is more homogenous and uniform as compared to center plane measurements. It is also seen a small region of low turbulence level in the mid-height of the fence, but not much low as the turbulence level resulted from the major jet along the center plane of the FSG fence.

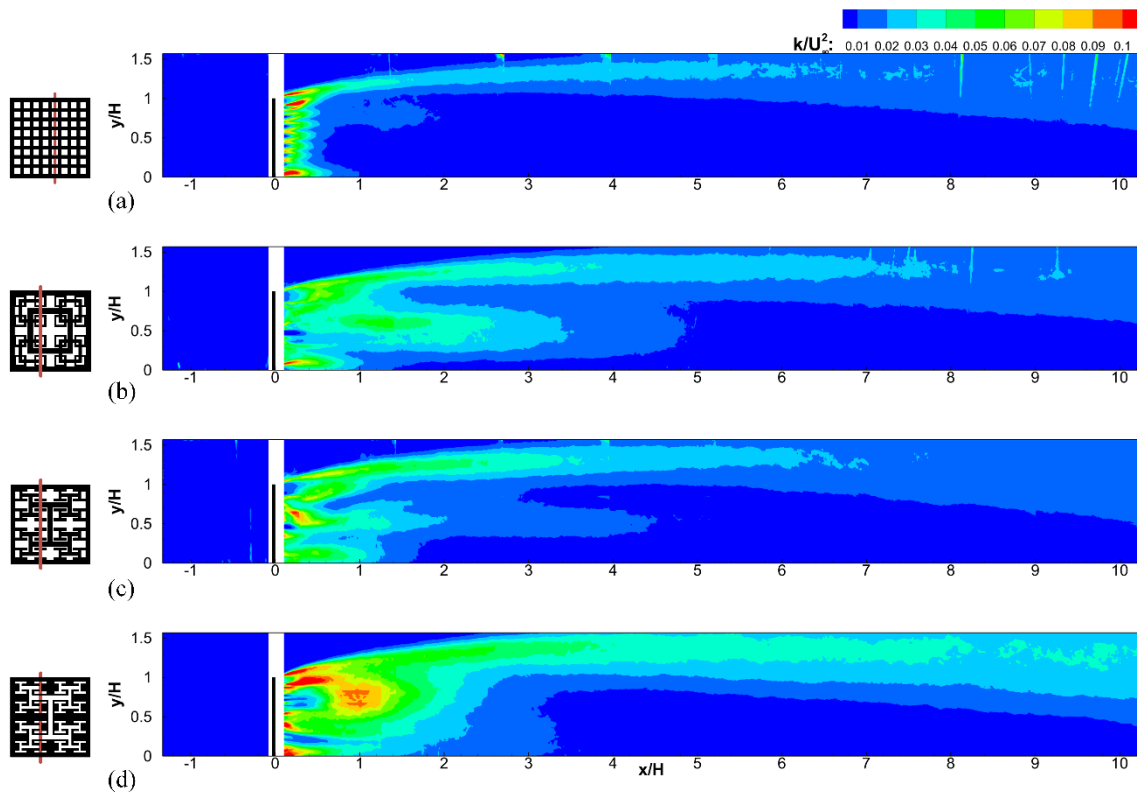


Figure 3-17 Normalized turbulent kinetic energy distributions downstream of (a) CSG, (b) FSG, (c) FIG and (d) FRIG fences based on the 2<sup>nd</sup> plane measurements

The FIG fence shown in Figure 3-16 (c) and Figure 3-17 (c) have completely different near wake turbulence level. According to center plane results two interesting observations to note are; first within the near wall region, especially within the small reversed flow region between  $2 < x/H < 4$  that was observed in the streamwise velocity distributions, the turbulence levels are quite low; second, the decay of turbulence seems to be much slower for the FIG fence such that even at  $x/H=6$  around  $y/H=0.5$ , relatively high levels of turbulence can be observed compared to the CSG and FSG cases. According to 2<sup>nd</sup> plane measurements, within the small reversed flow region, the turbulence level are relatively low as in the case of the center plane measurements. However, after  $5H$  downstream distance from the FIG fence, the decay of turbulence level is similar to those of CSG and FSG cases.

The FRIG fence presented in Figure 3-16 (d) and Figure 3-17 (d) seems to be generating the highest amount of turbulence within its near wake compared to other fence types based on both center and 2<sup>nd</sup> plane measurements. The second plane measurements have higher turbulent kinetic energy in the near wake as compared with the results of the center plane measurement of FRIG. Besides, the high turbulence shear layer along the upper wake boundary seems to be the largest among all fences. Nevertheless, the decay of turbulent kinetic energy is observed to be faster than FSG and FIG fences within the region that after about  $x/H=3.5$  the turbulence level are already reduced down to free-stream levels within the large portion of the wake.

Figure 3-18 and Figure 3-19 present the vertical profiles of the normalized mean turbulent kinetic energies of the fences measured at different locations. As can be seen from these figures, CSG fence has the lowest turbulent kinetic energy among four different fences. In the near wake region where  $x<2H$ , FRIG fence gives the highest levels of turbulent kinetic energy. Also, it is observed that FRIG fence has higher turbulent kinetic energies along its 2<sup>nd</sup> plane. As the distance increases along downstream direction, turbulent kinetic energies of the fences decrease gradually.

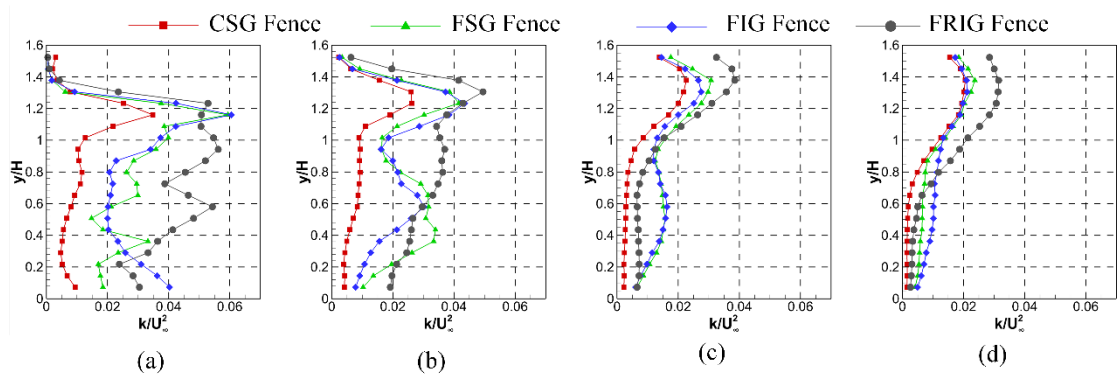


Figure 3-18 Normalized turbulent kinetic energy profiles at (a)  $x=H$ , (b)  $x=2H$ , (c)  $x=4H$  and (d)  $x=6H$ ; for CSG, FSG, FIG and FRIG fences based on the mid-plane measurements

Although fractal geometry differences are visible at 4H distance behind the fences along their mid-planes, the differences in the turbulent kinetic energy profiles decrease along the 2<sup>nd</sup> plane at the same distance, 4H.

After 6H distance, the effect of shear layers of the fences still affect the profiles and after  $y/H < 1$  FRIG fence still have higher level of turbulence according to both center and second plane measurements.

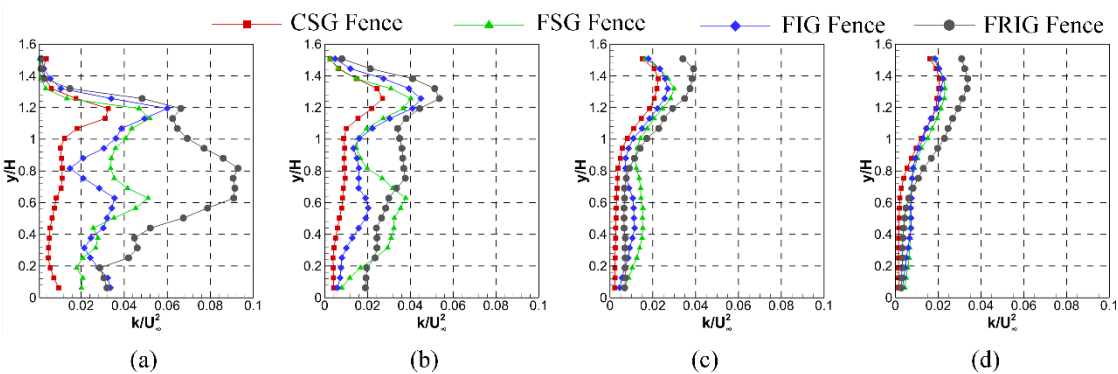


Figure 3-19 Normalized turbulent kinetic energy profiles at (a)  $x=H$ , (b)  $x=2H$ , (c)  $x=4H$  and (d)  $x=6H$ ; for CSG, FSG, FIG and FRIG fences based on the 2<sup>nd</sup> plane measurements

### 3.4 Wind Comfort Characteristics

Efficiency in wind speed reduction can be evaluated by the wind speed reduction coefficient which is first proposed by Cornelis and Gabriels [19] as follows:

$$Rc_{\Delta x,y} = 1 - \frac{u_{\Delta x,y}}{u_{0\Delta x,y}} \quad (3-2)$$

where  $\Delta x$  is the distance from the fence in terms of fence height,  $y$  is the height above the surface in terms of fence height,  $u_{\Delta x,y}$  is the time-averaged wind speed in the existence of fence, and  $u_{0\Delta x,y}$  is the time-averaged wind speed without the existence of fence.

Contour plots of wind speed reduction coefficient for all fences are shown in Figure 3-20 and Figure 3-21 based on center and 2<sup>nd</sup> plane measurements, respectively. In these figures, negative values of wind speed reduction coefficient are seen in dark blue color. It indicates that at these locations, wind speed is higher than the wind speed measured without existence of the fence. High values of wind speed reduction on the other hand, show high amount of reduction at these locations, which are shown with red color.

The baseline case of this study, CSG fence, results a homogenous distribution of the wind speed reduction coefficient shown in Figure 3-20 (a) and Figure 3-21 (a). In the region where  $x < 1H$ , wind speed decreases approximately 50%. It reaches to a range 0.5-0.6 of wind speed reduction in between 1H and 2H distance from the fence. On the other hand one can observe that FSG and FIG fences give much higher values of wind speed reduction coefficient near the wall and starting closer to the fence. After 2H distance where jet flows through the openings of the CSG fence fully mix, a large quiet zone begin to grow. In this region, the wind speed reduces up to 0.7-0.8.

However, the height of this quiet zone decreases gradually after  $2.5H$  distance from the fence. At  $10H$  distance from the fence, the height of this quiet zone is about  $0.6H$ .

It is observed from Figure 3-20 (b) and Figure 3-21 (b) that the large opening in the middle of the FSG fence results an increase in the streamwise velocity which directly affect the wind speed reduction coefficient and cause decrease in wind speed reduction coefficient, which is not desirable. However, there exists a quiet zone in which wind speed reduction coefficient is higher than 0.8 in between  $1H$  and  $5H$  distance downstream of the fence. Although the height of the quiet zone of FSG fence is not higher than  $0.5H$ , quite high values of reduction in wind speed is obtained. Also, contrary to quiet zone of the conventional fence, height of the quiet zone of the FSG increases as distance increases from the fence.

Maximum reduction in wind speed reduction is achieved by FIG fence based on both center and second plane measurements, shown in Figure 3-20 and Figure 3-21, respectively. There exist a quiet zone where the wind speed is almost fully reduced (Figure 3-20 (c) and Figure 3-21 (c)). This region is extended from  $1.5H$  to  $5H$  in the longitudinal direction and  $0.4H$  in the vertical direction from the tunnel bottom wall along the center plane. Along the 2<sup>nd</sup> plane however, this region begins after  $2H$  downstream of the fence and extends  $5H$  along the longitudinal direction. Also, it can be seen that considerably high amount of reduction is obtained using FIG fence, which is higher than 0.8, and it extends even more than  $10H$  in longitudinal distance behind the fence. As can be seen from 2<sup>nd</sup> plane measurements in Figure 3-21 (c), the height of the outer region of the quiet zone remains almost constant in which wind speed reduced more than 80%. Also, there exit a third outermost region of the quiet zone in which wind speed decreased in a 0.7-0.8 band, and the height of this region is  $0.7H$  along the 2<sup>nd</sup> plane. The main reason behind this relatively large region with high values of wind speed reduction coefficient is different flow structures that are created within the near wake of the FIG fence, such as high positive transverse velocity zone that forces the flow momentum near the wall to be significantly reduced, as explained in detail in previous sections.

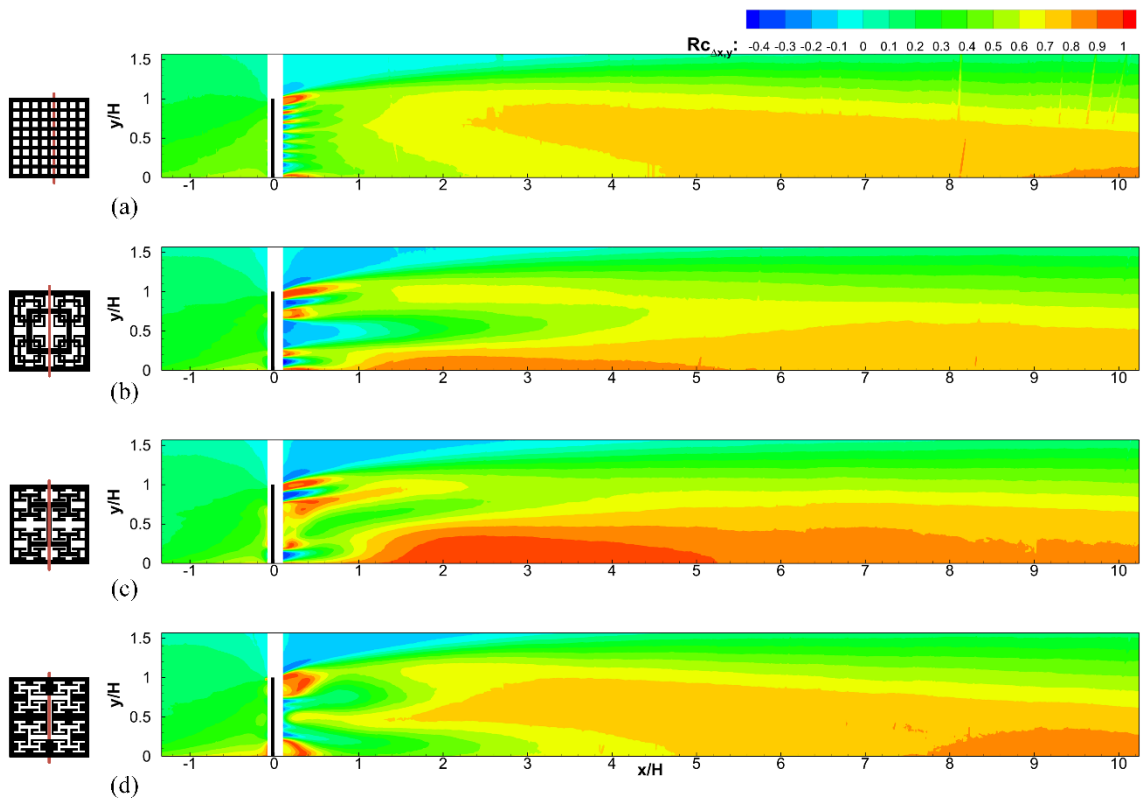


Figure 3-20 Wind speed reduction coefficient (equation 3-2) distribution of (a) CSG (b) FSG (c) FIG and (d) FRIG fences based on center plane measurements

A very similar distribution of wind speed reduction coefficient is seen for FRIG and CSG fences after a  $3H$  distance downstream of the fences. Similar to CSG fence, there exist a large quiet zone but its height is gradually decreases as in the case of CSG fence. In this region wind speed is decreased more than 0.7. Nevertheless, a smaller quiet zone still exists after  $x/H > 8$  extending down to  $x/H = 10$  in which wind speed reduction coefficient is higher than 0.8, as can be seen from Figure 3-20 (d) and Figure 3-21 (d).

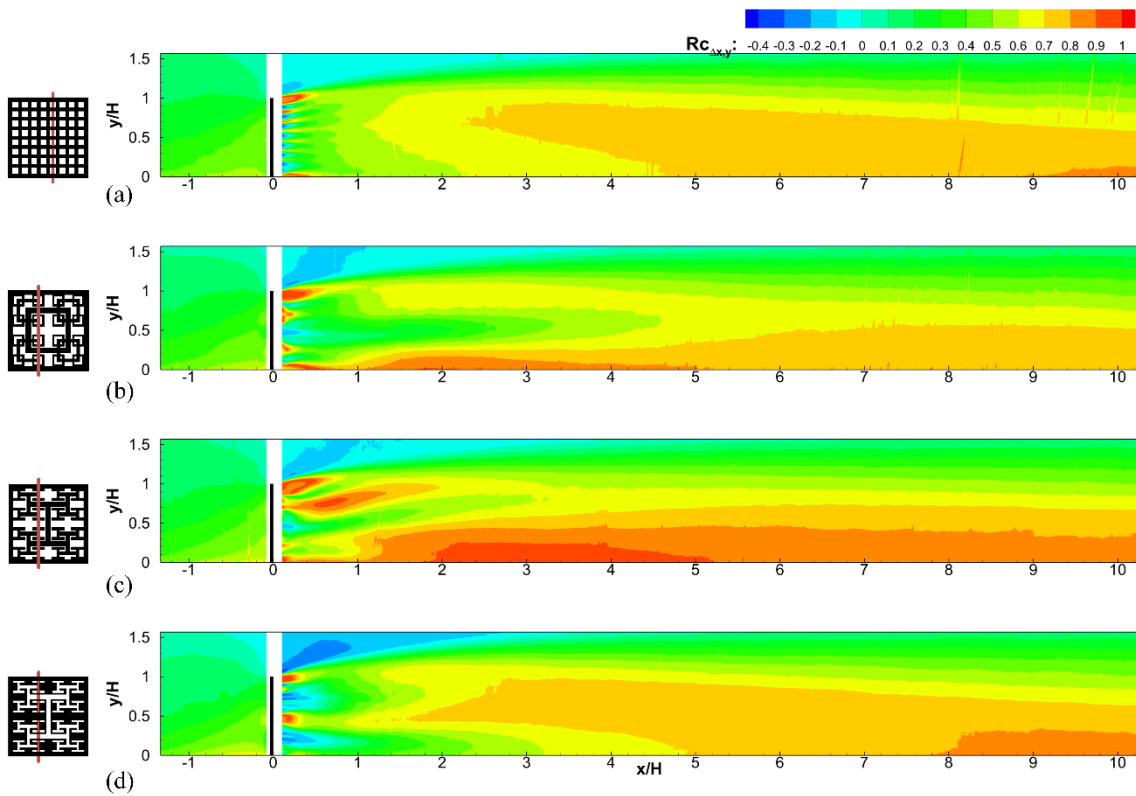


Figure 3-21 Wind speed reduction coefficient (equation 3-2) distribution of (a) CSG (b) FSG (c) FIG and (d) FRIG fences based on 2<sup>nd</sup> plane measurements

Figure 3-22 and Figure 3-23 show the variation of wind speed reduction coefficient along  $x/H$  at four different  $y/H$  locations. It is observed that at the far wake regions where  $x > 8H$ , wind speed reduction distributions are not much different than each other for different fence types. This holds for both center plane and 2<sup>nd</sup> plane results. However, for the near wake region where  $x < 2H$ , different geometries of fences directly affect the distributions except that along the  $y = 1.0H$  planes. It is also observed that as the distance increases vertically from the tunnel bottom wall, the differences in wind speed reduction coefficient distributions decrease. Also, it is interesting to see that very similar wind speed reduction distributions are obtained from the center and 2<sup>nd</sup> plane measurements.

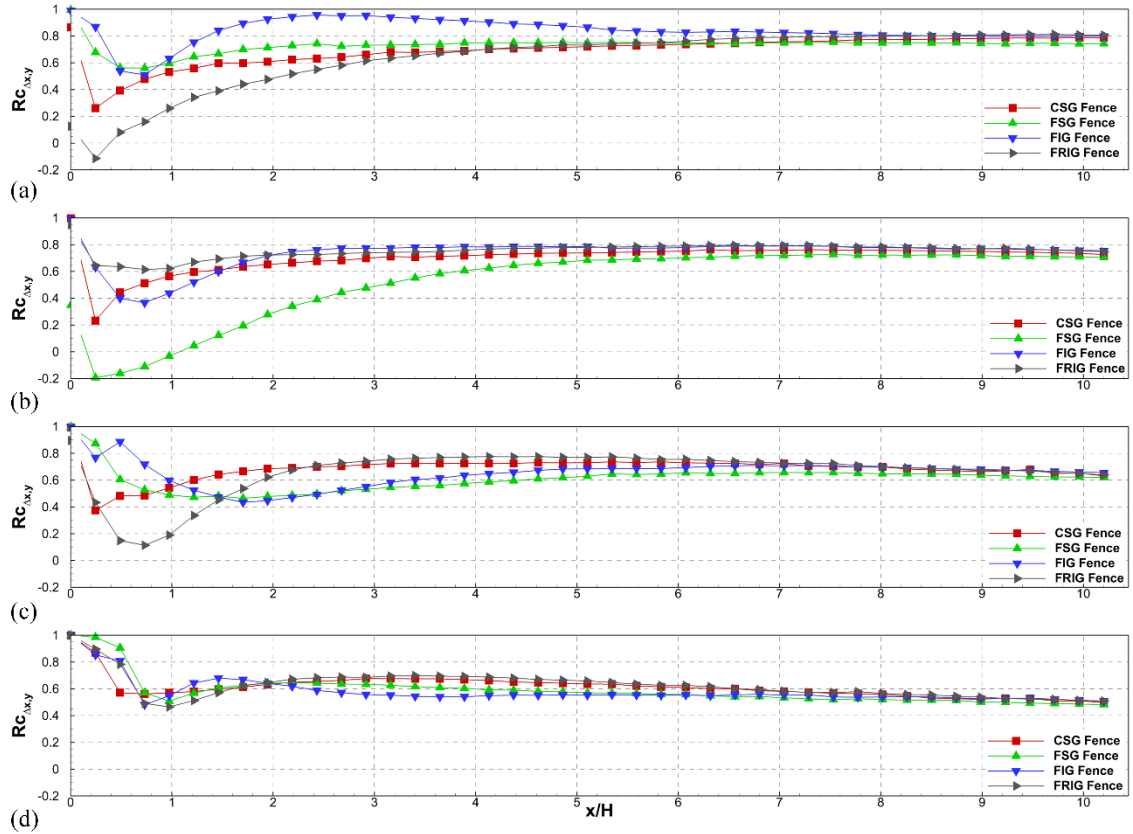


Figure 3-22 Wind speed reduction coefficient distributions along  $x/H$  at (a)  $y=0.25H$ , (b)  $y=0.50H$ , (c)  $y=0.75H$  and (e)  $y=1.0H$  based on center plane measurements

At  $y/H = 0.25$  shown in Figure 3-22 (a) and Figure 3-23 (a), almost all locations along  $x/H$ , the FIG fence gives the maximum wind speed reduction. It is also observed that FSG fence has higher wind speed reduction than CSG fence. On the other hand, FRIG fence results in the lowest reduction in wind speed reduction up to  $4H$  distance from the fence. After about  $x/H=4$  in center plane results and  $x/H=3$  in second plane results, the wind speed reduction levels of the FRIG quickly catch up to levels of CSG and FSG fences. After  $8H$  distance in the longitudinal direction, CSG and fractal fences converges to 80% reduction in the wind speed.

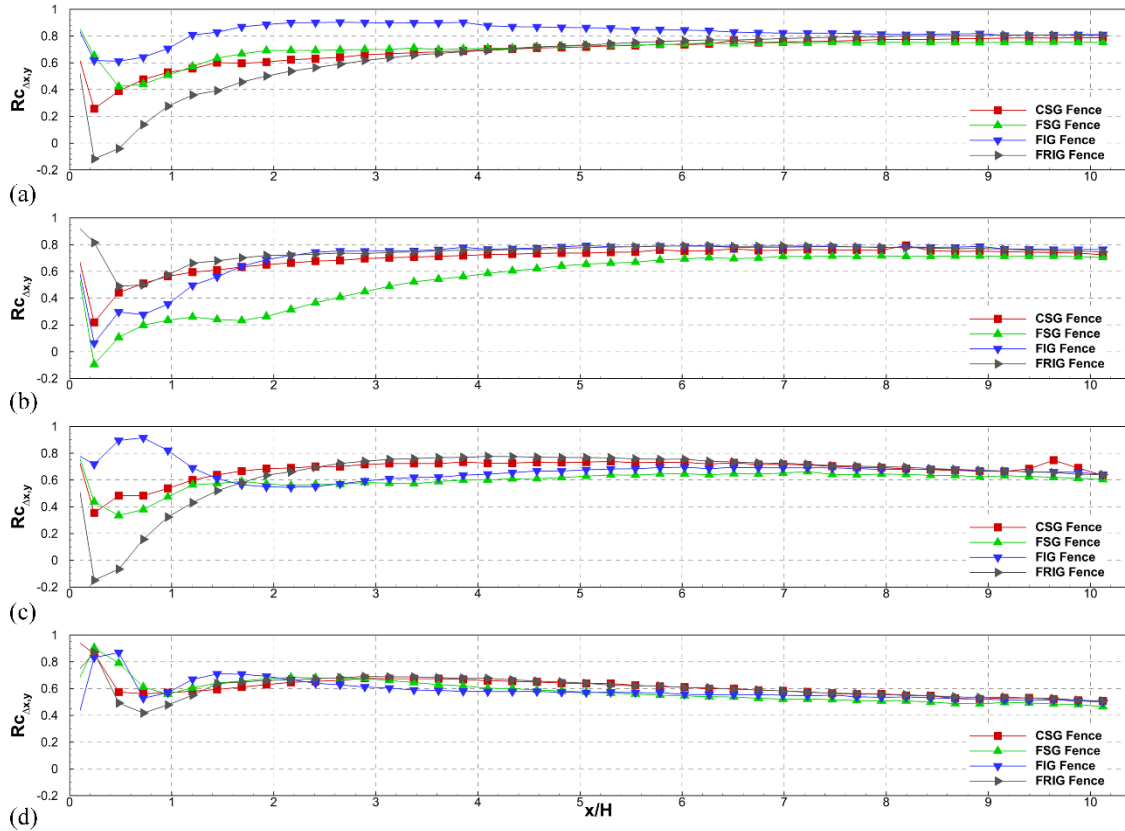


Figure 3-23 Wind speed reduction coefficient distributions along  $x/H$  at (a)  $y=0.25H$ , (b)  $y=0.50H$ , (c)  $y=0.75H$  and (e)  $y=1.0H$  based on  $2^{\text{nd}}$  plane measurements

According to center and  $2^{\text{nd}}$  plane measurements, at the  $y/H=0.50$ , the maximum reduction in wind speed (about 70%) is achieved by FRIG fence (Figure 3-22 (b) and Figure 3-23 (b)) in the near wake region. On the other hand, FSG fence exhibits a dramatic decrease in the wind speed reduction, which can be observed in both Figure 3-22 (b) and Figure 3-23 (b). This is due to the jet flow existing in the center of the FSG fence. Except for the near wake region  $x < 2H$ , FIG fence also results higher reduction compared to CSG fence.

Along  $y=0.75$  section, shown in Figure 3-22 (c) and Figure 3-23 (c), FRIG fence is the best option among all fences after a  $2H$  distance behind the fence. In the  $2 < x/H < 4$ , FSG and FIG fences show approximately 50% reduction in wind speed, while it is about 75% for CSG and FRIG fences.

At the height of  $y=1H$ , all four fences exhibit very similar trend in the near fence region ( $x<2H$ ) as it is seen in Figure 3-22 (d) based on center plane measurements. On the other hand, 2<sup>nd</sup> plane measurements show a small increase in wind speed reduction for the FSG and FIG fences in the region where  $x/H<0.5$ . In the range of  $2<x/H<4$ , FIG fence has slightly smaller reduction of wind speed among all fences. In total, FRIG fence gives highest reduction along the longitudinal direction. However, as can be seen from Figure 3-22 (d) and Figure 3-23 (d), the variations becomes not much as lower plane values e.g. for  $y/H=0.25$  plane.

It is obvious that these trends will have a significant impact in terms of required transverse extent (i.e. along  $y/H$ ) of effectiveness of the fence in terms of wind speed reduction in actual implementations.

In addition to the wind speed reduction coefficient, shelter parameter is another means of quantitative evaluation of wind comfort as proposed by Kim and Lee [29]:

$$\Psi = \frac{|u| + \sqrt{u'^2} + |v| + \sqrt{v'^2}}{U_0 + \sqrt{u_0'^2}} \quad (3-3)$$

where  $u$  is the mean streamwise velocity and  $v$  is the transverse velocity in the disturbed flow caused by fence,  $\sqrt{u'^2}$  and  $\sqrt{v'^2}$  are the corresponding standard deviations.  $U_0$  is the mean streamwise velocity in the absence of fence and  $\sqrt{u_0'^2}$  is its standard deviation.

As shown in Equation 3-3, this dimensionless parameter counts on both streamwise and vertical velocities and their standard deviations. Although, transverse velocity levels and their standard deviations are in general smaller compared to those of the streamwise velocity component, it is important to take them into account in order to obtain an accurate shelter parameter [29]. Note that low values of the shelter parameter are desired.

Shelter parameter distributions for fences are given in Figure 3-24 and Figure 3-25 based on center and 2<sup>nd</sup> plane measurements, respectively. It is observed that in the near wake region where  $x/H < 2$ , CSG fence results the lower values for the shelter parameter, which indicates a better shelter performance than fractal fences. This is mainly because of the fact that fractal fences have higher transverse velocity levels in this region due to complex and non-uniform near wake flow features, as discussed in detail in the previous sections.

Figure 3-24 (a) and Figure 3-25 (a) present the shelter parameter distribution of the CSG fence. It is seen from the figures there exist a sheltered region in which shelter parameter is lower than 0.4. Also at the far downstream, a small sheltered region (in  $6.2 < x/H < 10.2$ ) exist in which shelter parameter is even smaller than 0.3.

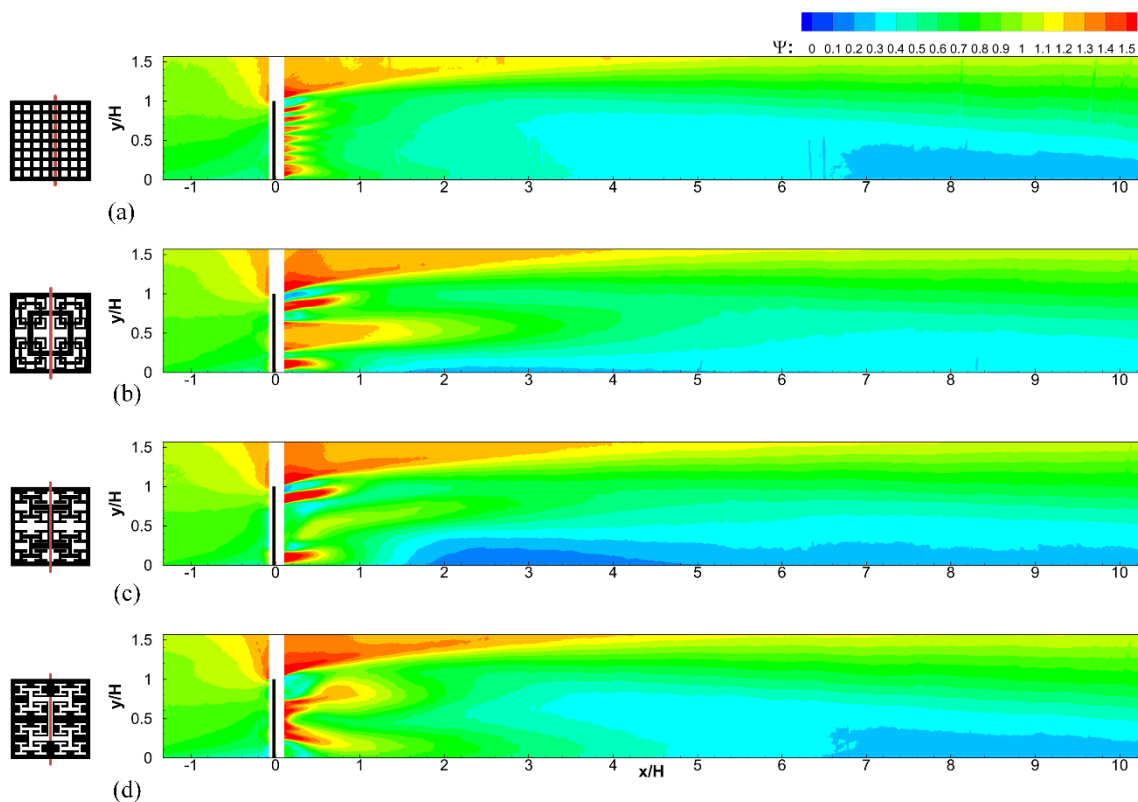


Figure 3-24 Shelter parameter (equation 3-3) distributions of (a) CSG (b) FSG (c) FIG and (d) FRIG fences based on center plane measurements

Similar to the wind speed reduction coefficient case, jet flow through the center of the FSG fence negatively effects the shelter parameter as can be seen from Figure 3-24 (b) and Figure 3-25 (b). In this case, although standard deviations of the streamwise and transverse velocities are not high, the increase in the streamwise velocity dominates this region generating higher values of the shelter parameter, which is not desirable. On the other hand, as can be seen from Figure 3-24 (b) and Figure 3-25 (b), there exist highly sheltered region in which shelter parameter is lower than 0.3 at low  $y/H$  locations.

Shelter parameter contour plots for FIG fence are given in Figure 3-24 (c) and Figure 3-25 (c). Based on center and 2<sup>nd</sup> plane measurements, FIG fence gives the best performance among other two fractal and CSG fences. The quiet zone behind the FIG fence is observed in which shelter parameter is lower than 0.2. Besides, there exist a long narrow region extending far distances from the fence in which shelter parameter values pretty small which shows the efficiency in the wind comfort.

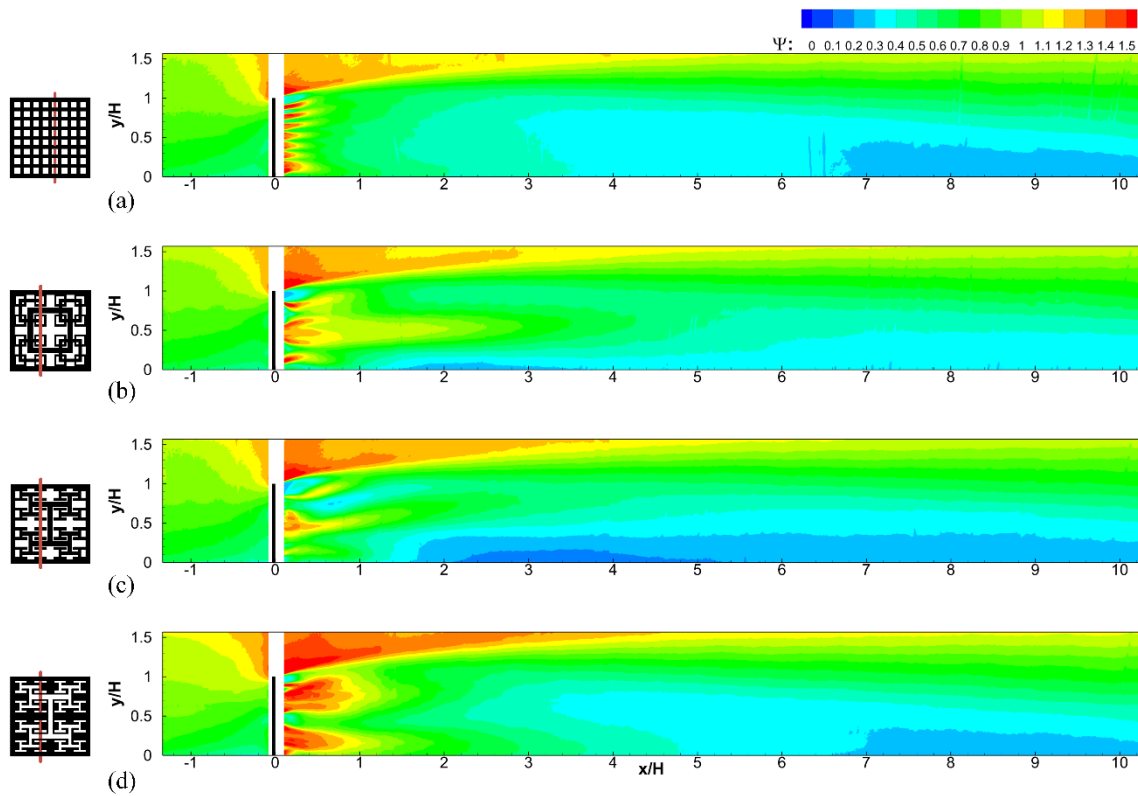


Figure 3-25 Shelter parameter (equation 3-3) distributions of (a) CSG (b) FSG (c) FIG and (d) FRIG fences based on 2<sup>nd</sup> plane measurements

In the region after about  $x/H=4$ , FRIG and CSG fence behaves in a similar way, which can be seen from Figure 3-24 (d) and Figure 3-25 (d). Although there exist a clear difference in the near wake region where  $x/H < 2$  in which fractal geometry dominates the flow pattern, after the near wake region this difference becomes smaller according to both center and 2<sup>nd</sup> plane measurements.

Shelter parameter distributions along four different transverse cross sections are shown in Figure 3-26 and Figure 3-27. As can be seen from these figures, as the downstream distance increases from the fences, the shelter parameter values for each fence collapse on top of each other especially after about  $x/H=8$  at all  $y/H$  locations and shelter parameter become almost negligible.

At  $y/H=0.25$  section, FIG fence gives the maximum shelter effect among four fences along longitudinal direction as shown in Figure 3-26 (a) and Figure 3-27(a). In the quiet zone of FIG fence, high degree of shelter is observed, where shelter parameter values are reduced almost down to 0.20. Further downstream, all four fences reveal quite high degree shelter ( $\Psi \approx 0.3$ ) in the range between  $6 < x/H < 10$ .

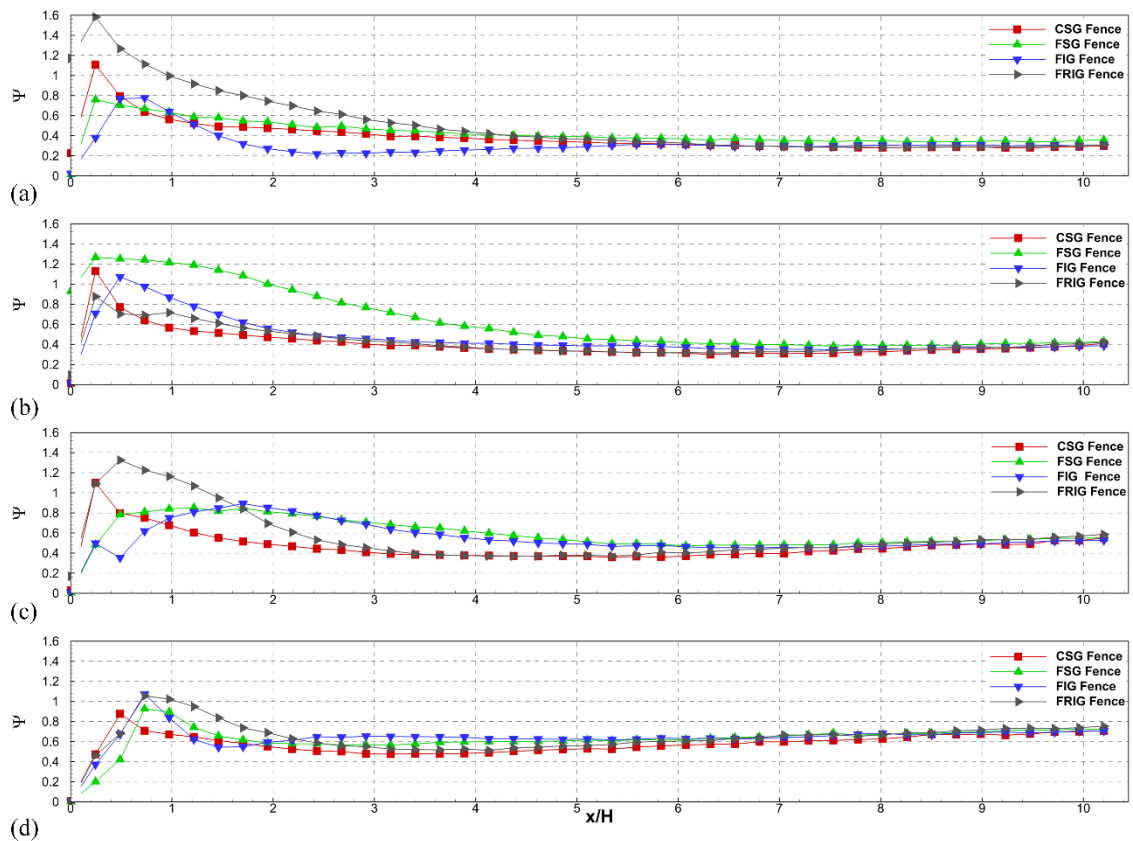


Figure 3-26 Shelter parameter distributions along  $x/H$  at (a)  $y=0.25H$ , (b)  $y=0.50H$ , (c)  $y=0.75H$  and (e)  $y=1.0H$  based on center plane measurements

At the mid-height plane ( $y/H=0.5$ ), CSG, FIG, and FRIG fences all show very similar trends as shown in Figure 3-26 (b) and Figure 3-27 (b). A shelter parameter value of 0.3 to 0.4 is obtained after  $2H$  distance behind these fences and this continues up to

end of our experiment domain. Similar to the wind speed reduction characteristics, due to the strong jet flow at the mid-plane of the CSG fence, the shelter parameter levels in the near wake zone are quite high, which is not desirable. When the effect of this jet flow diminishes after about  $x/H=6$ , FSG fence shows similar levels with the other three fences.

At  $y/H = 0.75$ , shown in Figure 3-26 (c) and Figure 3-27(c), FRIG fence and CSG fence show slightly smaller shelter parameter values compared with the others in the range of  $3 < x/H < 7$ . After about  $x/H=7$ , the differences becomes almost negligible in the shelter performance for all four fences.

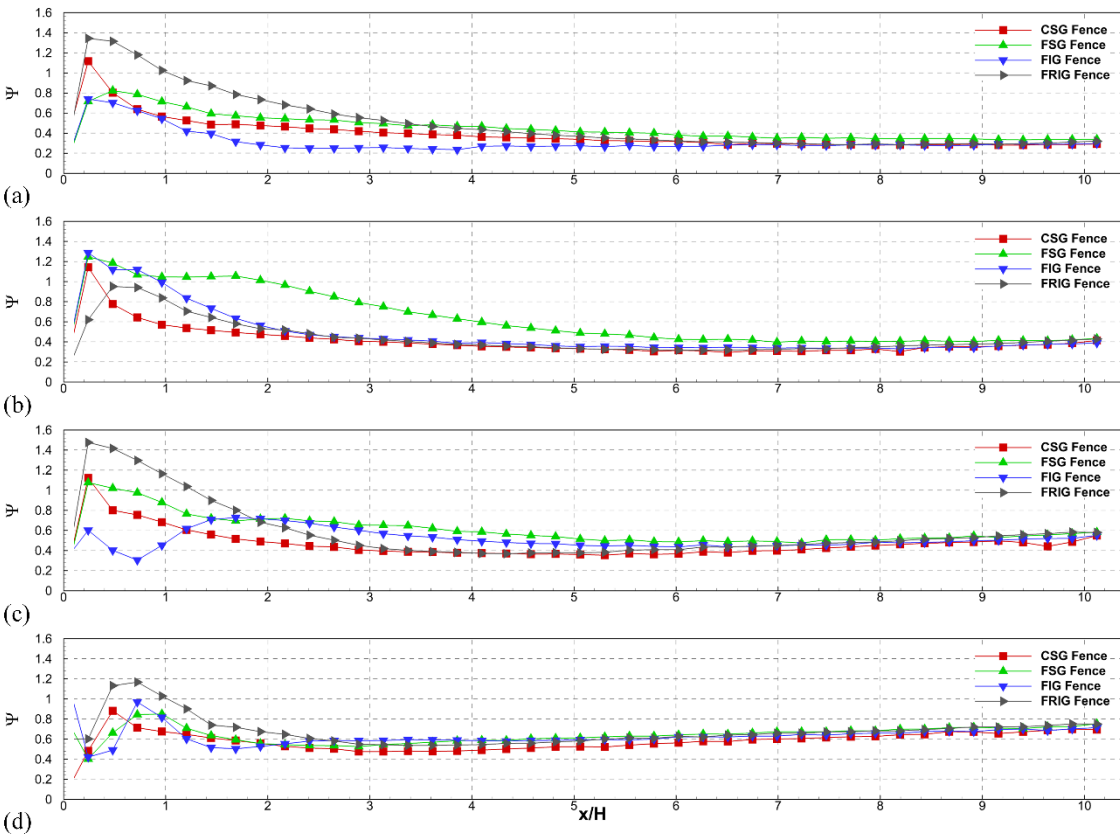


Figure 3-27 Shelter parameter distributions along  $x/H$  at (a)  $y=0.25H$ , (b)  $y=0.50H$ , (c)  $y=0.75H$  and (e)  $y=1.0H$  based on 2<sup>nd</sup> plane measurements

In the last transverse cross section ( $y/H=1$ ), similar results with the wind speed reduction distribution appears as shown in Figure 3-26 (d) and Figure 3-27(d). The distribution profiles along the longitudinal axis show very small variations from fence to fence. They reach a shelter parameter value of approximately 0.60 in the range  $2 < x/H < 8$ . After  $8H$  distance from the fences, shelter value reaches a value about 0.7.



## CHAPTER 4

### CONCLUSIONS

Two-dimensional PIV measurements around four different wind fences (conventional square, fractal square, fractal I and fractal reverse-I grid fences) were conducted in a wind tunnel to examine the turbulent flow field characteristics and to compare shelter effectiveness of the fractal wind fences. Results are based on two different sets of experiments for each fractal fences, one of them is measurements along the center plane, and the other is along the plane where all three geometric iterations intersect which is named as 2<sup>nd</sup> plane. It is detected that both set of experiments result very similar conclusions.

In the near wake region (i.e.  $x/H < 2$ ), the jets and wakes of various openings and bars that are present on specific fence grid geometries dominate the flow. While the flow is quite uniform and gets quickly mixed within the near wake of the conventional square grid fence, near wake regions of fractal fences display substantial non-uniformities both in streamwise as well as transverse directions. These non-uniformities and relevant jet-wake interactions set the level of turbulence and its decay characteristics as the flow convected downstream of the fences. Furthermore, these interactions also have a major impact on the effectiveness in wind protection, which heavily depend on features of the near wake flow fields.

Current results particularly show that the wake and jets flow patterns downstream of the fractal I grid fence create relatively long (i.e. along  $x/H$ ) and high (i.e. along  $y/H$ ) quiet zones with increased levels of wind reduction and high sheltering effects. If these jet-wake-wall interactions within the near wake are properly manipulated by custom designing fractal grid fences based on given wind comfort requirements, both mean flow as well as sheltering effects can potentially be adjusted for maximum benefit.

For the future study, an investigation of the effects of fractal parameters on the wake flow and wind comfort characteristics can improve the custom designing of fractal wind fences. Also, the results of fractal reverse-I grid fence indicate that this type of grid has a potential for mixing applications.

## REFERENCES

- [1] A. F. E. Wise, "Effects due to groups of buildings," *Philos. Trans. R. Soc.*, vol. A. 269, pp. 469–485, 1971.
- [2] W. H. Melbourne, "Criteria for Environmental Wind Conditions," vol. 3, pp. 241–249, 1978.
- [3] R. Baltaxe, "Air flow patterns in the lee of model windbreaks," *Arch. für Meteorol. Geophys. und Bioklimatologie Ser. B*, vol. 15, no. 3, pp. 287–312, 1967.
- [4] L. Hagen, E. Skidmore, P. Miller, and J. Kipp, "Simulation of effect of wind barriers on airflow," *Trans. ASAE*, vol. 24, no. 4, pp. 1002–1008, 1981.
- [5] H. Blanco-Canqui and R. Lal, "Principles of Soil Conservation and Management," in *Principles of Soil Conservation and Management*, 2008, pp. 55–80.
- [6] D. Guan, Y. Zhang, and T. Zhu, "A wind-tunnel study of windbreak drag," *Agric. For. Meteorol.*, vol. 118, no. 1–2, pp. 75–84, 2003.
- [7] B. Li and D. J. Sherman, "Aerodynamics and morphodynamics of sand fences: A review," *Aeolian Res.*, vol. 17, pp. 33–48, 2015.
- [8] Z. Dong, G. Chen, X. He, Z. Han, and X. Wang, "Controlling blown sand along the highway crossing the Taklimakan Desert," *J. Arid Environ.*, vol. 57, no. 3, pp. 329–344, 2004.
- [9] Z. Dong, W. Luo, G. Qian, and H. Wang, "A wind tunnel simulation of the mean velocity fields behind upright porous fences," *Agric. For. Meteorol.*, vol. 146, no. 1–2, pp. 82–93, 2007.
- [10] S. J. Lee, K. C. Park, and C. W. Park, "Wind tunnel observations about the shelter effect of porous fences on the sand particle movements," *Atmos.*

- Environ.*, vol. 36, no. 9, pp. 1453–1463, 2002.
- [11] J. L. Santiago, F. Martín, A. Cuerva, N. Bezdenejnykh, and A. Sanz-Andrés, “Experimental and numerical study of wind flow behind windbreaks,” *Atmos. Environ.*, vol. 41, no. 30, pp. 6406–6420, 2007.
- [12] S. J. Lee and H. B. Kim, “Laboratory measurements of velocity and turbulence field behind porous fences,” *J. Wind Eng. Ind. Aerodyn.*, vol. 80, no. 3, pp. 311–326, 1999.
- [13] A. D. Ferreira and R. J. Lambert, “Numerical and wind tunnel modeling on the windbreak effectiveness to control the aeolian erosion of conical stockpiles,” *Environ. Fluid Mech.*, vol. 11, no. 1, pp. 61–76, 2011.
- [14] L. Sun, Q. Zhao, J. Xiang, J. Shi, L. Wang, S. Hu, and S. Su, “Experimental and numerical study of fence effects on dust emission into atmosphere from open storage piles,” *Huagong Xuebao/CIESC J.*, vol. 18, pp. 411–419, 2011.
- [15] S. Charuvisit, K. Kimura, and Y. Fujino, “Effects of wind barrier on a vehicle passing in the wake of a bridge tower in cross wind and its response,” *J. Wind Eng. Ind. Aerodyn.*, vol. 92, no. 7–8, pp. 609–639, 2004.
- [16] H. Kozmar, L. Procino, A. Borsani, and G. Bartoli, “Optimizing height and porosity of roadway wind barriers for viaducts and bridges,” *Eng. Struct.*, vol. 81, pp. 49–61, 2014.
- [17] H. Kozmar, L. Procino, A. Borsani, and G. Bartoli, “Sheltering efficiency of wind barriers on bridges,” *J. Wind Eng. Ind. Aerodyn.*, vol. 107–108, pp. 274–284, 2012.
- [18] J. Wium, “Wind effect on structures: An introduction,” 2005.
- [19] W. M. Cornelis and D. Gabriels, “Optimal windbreak design for wind-erosion control,” *J. Arid Environ.*, vol. 61, no. 2, pp. 315–332, 2005.
- [20] G. M. Heisler and D. R. Dewalle, “2. Effects of windbreak structure on wind flow,” *Agric. Ecosyst. Environ.*, vol. 22–23, no. C, pp. 41–69, 1988.

- [21] M. D. A. E. S. Perera, “Shelter behind two-dimensional solid and porous fences,” *J. Wind Eng. Ind. Aerodyn.*, vol. 8, no. 1–2, pp. 93–104, 1981.
- [22] I. P. Castro, “Wake characteristics of two-dimensional perforated plates normal to an air-stream,” *J. Fluid Mech.*, vol. 46, no. 3, p. 599, 1971.
- [23] I. P. Castro, “Wake characteristics of two-dimensional perforated plates normal to an air-stream,” *J. Fluid Mech.*, vol. 46, no. 3, pp. 599–609, 1971.
- [24] J. K. Raine and Stevenson D. C., “Wind protection by model fences in a simulated atmospheric boundary layer,” *J. Ind. Aerodyn.*, vol. 2, pp. 159–180, 1977.
- [25] M. D. A. E. S. Perera, “Shelter behind two-dimensional solid and porous fences,” *J. Wind Eng. Ind. Aerodyn.*, vol. 8, pp. 93–104, 1981.
- [26] T. Tsukahara, Y. Sakamoto, D. Aoshima, M. Yamamoto, and Y. Awaguchi, “Visualization and laser measurements on the flow field and sand movement on sand dunes with porous fences,” *Exp. Fluids*, vol. 52, no. 4, pp. 877–890, 2012.
- [27] Z. Dong, G. Qian, W. Luo, and H. Wang, “Threshold velocity for wind erosion: The effects of porous fences,” *Environ. Geol.*, vol. 51, no. 3, pp. 471–475, 2006.
- [28] Z. Dong, W. Luo, G. Qian, and H. Wang, “Evaluating the optimal porosity of fences for reducing wind erosion,” *Engineering*, vol. 3, no. 1, pp. 0001–0012, 2011.
- [29] S. J. Kim, H. B.; Lee, “The structure of turbulent shear flow around a two-dimensional porous fence having a bottom gap,” *J. Fluids Struct.*, vol. 16, no. 3, pp. 317–329, 2002.
- [30] W. Dierickx, D. Gabriels, and W. Cornelis, “A wind tunnel study on wind speed reduction of technical textiles used as windscreen,” *Geotext. Geomembranes*, vol. 19, pp. 59–73, 2001.

- [31] A. Staicu, B. Mazzi, J. C. Vassilicos, and W. Van De Water, “Turbulent wakes of fractal objects,” *Phys. Rev.*, vol. 67, no. 6 2, 2003.
- [32] D. Hurst and J. C. Vassilicos, “Scalings and decay of fractal-generated turbulence,” *Phys. Fluids*, vol. 19, no. 19, pp. 25112–105108, 2007.
- [33] E. R. Seoud and C. J. Vassilicos, “Dissipation and decay of fractal-generated turbulence,” *Phys. Fluids*, vol. 19, no. 10, pp. 1–12, 2007.
- [34] S. Laizet and J. C. Vassilicos, “Multiscale generation of turbulence,” *J. Multiscale Model.*, vol. 1, no. 1, pp. 177–196, 2009.
- [35] S. Laizet and J. C. Vassilicos, “Fractal space-scale unfolding mechanism for energy-efficient turbulent mixing,” *Phys. Rev. E - Stat. Nonlinear, Soft Matter Phys.*, vol. 86, no. 4, pp. 1–5, 2012.
- [36] C. J. Keylock, K. Nishimura, M. Nemoto, and Y. Ito, “The flow structure in the wake of a fractal fence and the absence of an ‘inertial regime,’” *Environ. Fluid Mech.*, vol. 12, no. 3, pp. 227–250, 2012.
- [37] S. M. McClure, “Experimental investigation of turbulent flow induced by new-generation wind fences with multi-scale fractal structure,” Cleveland State University, 2016.
- [38] D. Hurst and J. C. Vassilicos, “Scalings and decay of fractal-generated turbulence,” *Phys. Fluids*, vol. 35103, no. 2007, pp. 0–31, 2007.
- [39] S. B. Pope, *Turbulent Flows*, vol. 1. 2000.